J Physiol 0.0 (2021) pp 1–23

# Connexin 46 and connexin 50 gap junction channel properties are shaped by structural and dynamic features of their N-terminal domains

Benny Yue<sup>1,\*</sup>, Bassam G. Haddad<sup>2,\*</sup>, Umair Khan<sup>2</sup>, Honghong Chen<sup>1</sup>, Mena Atalla<sup>1</sup>, Ze Zhang<sup>1</sup>, Daniel M. Zuckerman<sup>3</sup>, Steve L. Reichow<sup>2</sup> and Donglin Bai<sup>1</sup>

Edited by: David Wyllie & Jean-Claude Béïque

**Abstract** Connexins form intercellular communication channels, known as gap junctions (GJs), that facilitate diverse physiological roles, from long-range electrical and chemical coupling to coordinating development and nutrient exchange. GJs formed by different connexin isoforms harbour unique channel properties that have not been fully defined mechanistically. Recent structural studies on Cx46 and Cx50 defined a novel and stable open state and implicated the amino-terminal (NT) domain as a major contributor for isoform-specific functional differences between these closely related lens connexins. To better understand these differences, we constructed models corresponding to wildtype Cx50 and Cx46 GJs, NT domain swapped chimeras, and point variants at the 9th residue for comparative molecular dynamics (MD) simulation and electrophysiology studies. All constructs formed functional GI channels, except the chimeric Cx46-50NT variant, which correlated with an introduced steric clash and increased dynamical behaviour (instability) of the NT domain observed by MD simulation. Single channel conductance correlated well with free-energy landscapes predicted by MD, but resulted in a surprisingly greater degree of effect. Additionally, we observed significant effects on transjunctional voltage-dependent gating (Vi gating) and/or open state dwell times induced by the designed NT domain variants. Together, these studies indicate intra- and inter-subunit interactions involving both hydrophobic and charged residues within the NT domains of Cx46 and Cx50 play important roles in defining GJ open state stability and single channel conductance, and establish the open state Cx46/50 structural models as archetypes for structure-function

Benny Yue is an MSc student in the Department of Physiology and Pharmacology at Western University. His research in the Bai lab focuses on dual patch clamp analysis of gap junction channel voltage-dependent gating and unitary channel properties. Both artificially designed and naturally occurred human disease-linked gap junction variants are investigated to reveal molecular mechanisms of how gap junction channels control opening/closing, the rate of ion permeation and impairments of disease-linked variants. Bassam Haddad is a PhD candidate in the Department of Chemistry at Portland State University. His research utilizes molecular dynamics simulations and Markov-state modelling to investigate permeability and selectivity in gap junction channels, and extend the insights gained from structural investigations of connexin-46/50. Here, the use of *in* 





Check for updates

silico mutagenesis complements channel functional data, providing atomic-detail insights into the effects of protein dynamics on channel gating, open-state stability and ion permeation.

This article was first published as a preprint: Yue B, Haddad BG, Khan U, Chen H, Atalla M, Zhang Z, Zuckerman DM, Reichow SL, Bai D. 2020. Connexin 46 and connexin 50 gap junction channel open stability and unitary conductance are shaped by structural and dynamic features of their N-terminal domains. bioRxiv. https://doi.org/10.1101/2020.07.01.182584

<sup>&</sup>lt;sup>1</sup>Department of Physiology and Pharmacology, University of Western Ontario, London, Ontario, Canada

<sup>&</sup>lt;sup>2</sup>Department of Chemistry, Portland State University, Portland, OR, 97201, USA

<sup>&</sup>lt;sup>3</sup>Department of Biomedical Engineering, Oregon Health and Science University, Portland, OR, 97239, USA

<sup>\*</sup>B.Y. and B.G.H. contributed equally to this study.

studies targeted at elucidating GJ channel mechanisms and the molecular basis of cataract-linked connexin variants.

(Received 6 January 2021; accepted after revision 12 April 2021; first published online 20 April 2021)

Corresponding authors Dr D. Bai: Department of Physiology and Pharmacology, University of Western Ontario, London, Ontario, N6A 5C1, Canada. Email: donglin.bai@schulich.uwo.ca

Dr S. L. Reichow: Department of Chemistry, Portland State University, Portland, OR 97201, USA. Email: reichow@pdx.edu

### Introduction

Gap junctions (GJs) are a class of membrane channels that provide a direct passageway between neighbouring cells and facilitate the exchange of ions and small molecules (Saez et al. 2003; Goodenough & Paul, 2009). This type of cell-to-cell communication is facilitated by a unique channel architecture, whereby a continuous water-filled pore  $\sim$ 1.5 nm in diameter is formed between two opposing cell membranes, effectively coupling the cytoplasms of adjoined cells (Sosinsky & Nicholson, 2005). These direct passageways are essential for enabling fast transmission of electrical signals in the brain and heart and for facilitating long-range metabolic coupling in most tissues. Because of their important physiological roles, genetic mutations or pathological conditions that lead to aberrant channel function have been linked to a variety of human disease, including deafness, cataracts, peripheral neuropathy, cardiac arrhythmia, stroke, skin disorders and cancers (Aasen et al. 2016; Garcia et al. 2016; Delmar et al. 2017).

GJ intercellular channels are formed through the assembly of 12 integral membrane proteins called connexins. Six connexins oligomerize to form a hemichannel (also known as connexon) and two hemichannels from neighbouring cells can dock together to form a functional gap junction channel if they are docking-compatible (White et al. 1994b; Bai et al. 2018). All connexins are predicted to have the same topological structure, which includes four transmembrane helices (TM1-4), two extracellular loops (EC1 and EC2), an amino-terminal (NT) domain, a carboxyl terminus (CT) and a cytoplasmic loop (CL) (Sohl & Willecke, 2004). Humans express 21 connexin isoforms in a cell-type-specific fashion, possibly reflecting the need for unique channel functions that match the physiological demands of their environment. Adding to this diversity, different tissues often express more than one type of connexin, which may co-assemble into so-called heteromeric channels (mixed within the same hemichannel) and/or heterotypic channels (mixed between opposing hemichannels) (Koval et al. 2014; Bai et al. 2018). In this way, cells may fine-tune their GJ channel properties to control the synchronization of physiological activities or to maintain homeostasis.

It has been well established that GJs formed by different connexins display different channel properties, including distinct permeability to substrates, various rates of ion permeation, and gating control by a variety of factors, including intracellular protons, divalent cations and transjunctional voltage (V<sub>i</sub>) (Bukauskas & Verselis, 2004; Bargiello & Brink, 2009). Transjunctional voltage-dependent gating (also known as  $V_i$  gating) exists in all characterized GJs, and depending on the component connexins the resultant GJs could show various levels of gating extent, half deactivation voltage, gating charge (which determines gating sensitivity), and gating kinetics (Harris et al. 1981; Paul et al. 1991; Veenstra et al. 1994; Verselis *et al.* 1994; White *et al.* 1994*a*; Trexler *et al.* 1996; Oh et al. 1999; Musa et al. 2004). Similarly, different connexin GJs also show drastically different rates of ion permeation measured by single channel conductance  $(\gamma_i)$ , from a few pico-Siemens (pS) in Cx30.2 and Cx36 to 200-300 pS in Cx50 and Cx37 (Veenstra et al. 1994; Srinivas et al. 1999; Moreno et al. 2005; Bukauskas et al. 2006). Although such distinct channel functions are well established, the underlying molecular and structural mechanisms for controlling GJ channel gating and ion permeation have not yet been fully defined.

Early functional studies on  $\beta$ -type connexins, such as Cx26 and Cx32, revealed that the charged residues in the beginning portion of the NT domain (within the first 10 amino acid residues) are important in sensing the  $V_i$ , determining the  $V_i$  gating polarity, and probably serving as a gate to close the channel (Verselis et al. 1994; Purnick et al. 2000; Oh et al. 2004). Studies on Cx40, Cx46 and Cx50 or their orthologues (members of  $\alpha$  connexins) also showed the importance of charged residues in their respective NT domains in determining GJ gating polarity, channel open stability, chemical block and/or rate of ion permeation (Musa et al. 2004; Tong et al. 2004; Peracchia & Peracchia, 2005; Srinivas et al. 2005; Tong & Ebihara, 2006; Xin et al. 2010; Xin & Bai, 2013). However, studies on residues in Cx45 or Cx50 NT showed that exchange of charged residues with similar charge properties could also alter  $V_i$  gating properties, gating kinetics and/or the rate of ion permeation (Xin et al. 2012; Santos-Miranda et al. 2020), suggesting features in addition to the charge state of the NT domain play a role in these channel properties.

The structural mechanisms for how NT domains are anchored in an open conformation and the molecular interactions to stabilize/destabilize this domain are also not yet clear. Previous structural studies on a Cx26 M34A variant showed evidence that the NT domain of Cx26 could form a plug-like structure in the centre of the pore, probably representing a closed GJ structure (Oshima *et al.* 2007, 2011). However, due to the limited resolution of this study, the detailed NT domain interactions responsible for forming the plug were not resolved (Oshima *et al.* 2011).

Maeda et al. (2009) resolved the first high resolution (3.5 Å) crystal structure of human Cx26 GJ. In this structure, the NT domain folds into the GJ channel pore forming the narrowest part of the GJ channel, a position that could serve the role of V<sub>i</sub>-sensing, regulating ion permeation selectivity and rate, modulation by intracellular substrates, as well as gating to close the GJ channel (Maeda et al. 2009). However, molecular dynamics (MD) simulation studies using this Cx26 GJ structure indicate that the NT domain may not represent the open state, and required significant chemical modification and/or freezing the dynamics of the structure to explain experimental data (Kwon et al. 2011; Villanelo et al. 2017). Using single particle cryo-electron microscopy (cryo-EM), we resolved native sheep lens GJs, Cx46 and Cx50, at 3.4 Å resolution (Myers et al. 2018). The NT domains of these two  $\alpha$  connexins also folded into the vestibule of the GJ pore to form the narrowest part of the pore, but in this case the NT domain adopted a more regular amphipathic helical conformation, where hydrophobic resides were positioned to anchor the NT domain through hydrophobic packing interactions with TM1/TM2, resulting in a more stable open state conformation as compared to Cx26 (Myers et al. 2018). In addition to these conformational differences, charged residues could directly influence the electrostatic environment of the permeation pathway and several novel intra- and inter-subunit interactions were discovered in the NT domain and it is not clear if these interactions play a role in stabilizing/destabilizing the channel open state or  $V_i$  gating mechanism.

To explore these findings further and harmonize the functional study with our structural models, we combined MD simulation studies with a dual patch clamp technique to characterize GJ properties of sheep Cx46, Cx50, NT domain swapped chimeras (Cx46-50NT and Cx50-46NT) and single point variants (Cx46-R9N and Cx50-N9R). Our results showed well-correlated atomic models and experimentally measured channel properties, despite timescale limitations of all-atom MD simulations of this size (typically limited to ns to  $\mu$ s timescales) that prevented full characterization of GJ gating properties measured by patch clamp measurements (ms to s timescales). This combined approach revealed a novel gating model that is dependent not just on the charge

properties of the NT domain, but also the hydrophobic anchoring sites that we show structurally and functionally serve to stabilize (or destabilize) the NT gating domain, which we believe represents a new paradigm in our understanding of how GJ gating is modulated. In addition, we demonstrate how local salt bridge interactions between neighbouring NT domains are probably very important for modulating both the conductance and the  $V_i$  gating of Cx46 and Cx50 GJs. More broadly, this type of interaction suggests that cooperativity between neighbouring connexin subunits may play a previously unrecognized, yet important role in defining the gating properties of GJs. Taken together, we demonstrate that the combined MD simulation models and electrophysiological functional studies on Cx46/50 are very powerful in providing novel insights into the molecular and structural mechanisms governing the GJ gating properties, channel open state stability and energetics of ion permeation.

### **Methods**

#### Plasmid construction

Sheep Cx46 (Cx46, also known as Cx44) and Cx50 (Cx50, also known as Cx49) cDNA were synthesized and each of them was inserted into an expression vector, pIRES2-EGFP, with an untagged GFP reporter between the restriction enzyme sites, *XhoI* and *EcoRI* (NorClone Biotech Laboratories, London, Ontario). Cx46-IRES-GFP was used as a template for PCR cloning to generate the chimera, Cx46-50NT, in which the amino terminal (NT) domain of Cx46 was replaced by Cx50 NT domain and a missense variant Cx46-R9N. Similarly, Cx50-IRES-GFP was used as a template to generate Cx50-46NT and Cx50-N9R. The primers used to generate these chimeras and point variants are listed below.

Cx46-50NT: forward 5'ATGGGCGACTGGAGCTTCC TGGGGAACATCTTGGAGGAGGTGAATGAGCACTC CACTGTCATC3' and reverse 5'GATGACAGTGGAGT GCTCATTCACCTCCTCCAAGATGTTCCCCAGGAAG CTCCAGTCGCCCAT3'

Cx50-46NT: forward 5'ATGGGAGACTGGAGTTTCC TGGGGAGACTCCTAGAGAACGCCCAGGAGCACTC CACGGTCATC3' and reverse 5'GATGACCGTGGAG TGCTCCTGGGCGTTCTCTAGGAGTCTCCCCAGGA AACTCCAGTCTCCCAT3'

Cx46-R9N: forward 5'GACTGGAGCTTCCTGGGGA ACCTCCTAGAGAACGCCCAG3' and reverse 5'CTGG GCGTTCTCTAGGAGGTTCCCCAGGAAGCTCCAGT C3'

Cx50-N9R: forward 5'TGGAGTTTCCTGGGGAGAAT CTTGGAGGAGGTG3' and reverse: 5'CACCTCCTCC AAGATTCTCCCCAGGAAACTCCA3'

GFP fusion tagged Cx46 (Cx46-GFP), the chimera (Cx46-50NT-GFP) and point variant (Cx46-R9N-GFP)

4 B. Yue and others J Physiol 0.0

were generated by subcloning these construct into the EGFP expression vector (Kim *et al.* 2013). Mutagenesis was used to remove the stop codon from each of these vectors and ensure that the GFP was linked in frame with a peptide linker (LGILQSTVPRARDPPVAT) between Cx46 (or Cx46-50NT) and GFP.

#### Cell culture and transient transfections

GJ-deficient mouse neuroblastoma (N2A) cells (American Type Culture Collection, Manassas, VA, USA) were grown in Dulbecco's modified Eagle's medium (DMEM) (Life Technologies Corporation, Grand Island, NY, USA) containing 4.5 g/L D-(+)-glucose, 584 mg/L L-glutamine, 110 mg/L sodium pyruvate, 10% fetal bovine serum (FBS), 1% penicillin and 1% streptomycin, in an incubator with 5% CO<sub>2</sub> at 37°C (Sun et al. 2013). N2A cells were transfected with 1.0  $\mu g$  of a cDNA construct and 2  $\mu$ L of X-tremeGENE HP DNA transfection reagent (Roche Diagnostics GmbH, Indianapolis, IN, USA) in Opti-MEM + GlutaMAX-I medium for 4 h. After transfection, the medium was changed back to FBS-containing DMEM and incubated overnight. The next day, N2A cells transfected with Cx46 and its variants were replated onto glass coverslips for 2 h before transferring to the recording chamber. N2A cells transfected with Cx50 and its variants were replated onto glass coverslips for 10 h before transferring to the recording chamber. Isolated green fluorescent cell pairs were selected for patch clamp study of homotypic GJs.

### Electrophysiological recording

Glass coverslips with transfected cells were placed into a recording chamber on an upright microscope (BX51WI, Olympus). The chamber was filled with extracellular solution (ECS) at room temperature (22–24°C). The ECS contained (in mM): 135 NaCl, 2 CsCl, 2 CaCl<sub>2</sub>, 1 MgCl<sub>2</sub>, 1 BaCl<sub>2</sub>, 10 HEPES, 5 KCl, 5 D-(+)-glucose, 2 sodium pyruvate, pH adjusted to 7.4 with 1 M NaOH, and osmolarity of 310-320 mOsm. Dual whole cell patch clamp was performed on green fluorescent cell pairs with a MultiClamp 700A amplifier (Molecular Devices, Sunnyvale, CA, USA). Patch pipettes were pulled with a micropipette puller (PC-10, Narishige International, Amityville, NY, USA) and filled with intracellular solution (ICS) containing (in mM): 130 CsCl, 10 EGTA, 0.5 CaCl<sub>2</sub>, 5 Na<sub>2</sub>ATP, 10 HEPES, adjusted to pH 7.2 with 1 M CsOH, and osmolarity of 290-300 mOsm. After establishing whole cell recording on the cell pair, both cells were voltage clamped at 0 mV. In one cell of the pair, a series of voltage pulses ( $\pm 20$  to  $\pm 100$  mV) were applied to establish transjunctional voltage  $(V_i)$ . The other cell of the pair was constantly held at 0 mV to record gap junctional current  $(I_j)$ . The current was low-pass filtered (Bessel filter at 1 kHz) and recorded using pClamp9.2 software at a sampling rate of 10 kHz via an AD/DA converter (Digidata 1322A, Molecular Devices).

### Transjunctional voltage dependent gating

Transjunctional voltage  $(V_i)$ -dependent gating  $(V_i \text{ gating})$ was studied in cell pairs expressing one of the constructs. Voltage pulses ( $\pm 20$  to  $\pm 100$  mV with 20 mV increment) were delivered in one cell of the pair to establish  $V_i$  values and transjunctional currents  $(I_j)$  were recorded in the other cell. In most cases,  $I_i$ s peaked at the beginning and then deactivated (especially with high  $V_i$  values,  $\pm 40$  to  $\pm 100$  mV) to a steady-state near the end of a 7 s  $V_i$ pulse. Gap junctional conductance  $(G_i)$  was calculated  $(G_i = I_i/V_i)$ . The steady state  $G_i$  was normalized to the peak G<sub>i</sub> to obtain a normalized steady-state junctional conductance  $(G_{j,ss})$  for each tested  $V_j$ . The  $G_{j,ss}$  values were then plotted with  $V_i$  values to obtain a  $G_{i,ss}$ – $V_i$  plot, which could sometimes fit well with a two-state Boltzmann equation for each  $V_i$  polarity to obtain gating parameters,  $V_0$ ,  $G_{\min}$ ,  $G_{\max}$  and A (Jassim *et al.* 2016).  $V_0$  is the voltage when the  $G_{\rm j,ss}$  is reduced by half [( $G_{\rm max}-G_{\rm min}$ )/2],  $G_{\rm min}$ is the normalized minimum residual conductance, while  $G_{\text{max}}$  represents the maximum normalized conductance, and A is the slope of the curve which reflects  $V_i$  gating sensitivity (Spray et al. 1981):

$$G_{j,ss} = \frac{G_{max} - G_{min}}{1 + \exp\left[A(V_j - V_0)\right]} + G_{min}$$
 (1)

### Single channel analysis

Single channel current  $(i_j)$  could be observed in cell pairs with few active GJ channels. The recorded currents were further filtered using a low-pass Gaussian filter at 200 Hz in Clampfit9.2 for measuring current amplitude and display in figures. The amplitude  $i_j$  values for the fully open state at different  $V_j$  values were measured with fitting Gaussian functions on all point current amplitude histograms. The  $i_j$  values of different cell pairs were averaged under the same  $V_j$ , regardless of  $V_j$  polarity, to generate a  $i_j$ – $V_j$  plot. Linear regression of the  $i_j$ – $V_j$  plot with at least four different  $V_j$  values was used to estimate slope unitary GJ channel conductance (also known as single channel conductance,  $\gamma_j$ ).

Single GJ channel open dwell times were analysed on cell pairs with only one active GJ channel. In this case, single channel currents were filtered with a low-pass Gaussian filter at 500 Hz (Clampfit9.2). The open dwell time was measured at the  $V_{\rm j}$  values from  $\pm 40$  to  $\pm 100$  mV using Clampfit9.2. Any single channel open events with less than 2 ms were excluded from the analysis as this is

beyond the resolution of our single channel recordings. The average open dwell time at each  $V_j$  was calculated and plotted for comparison. The total number of open events for Cx50 and Cx50-N9R GJs was a lot higher than other GJs and suitable for more in-depth analysis on the open dwell times. Histograms of Cx50 and Cx50-N9R were plotted in a logarithmic scale with five bins per decade and fitted with a two-exponential probability fitting (Ramanan *et al.* 1999). The two time constant  $(\tau)$  values represent the corresponding open dwell times for each of the peaks in the fitting. The  $\tau_{\rm mean}$  value was calculated by taking the weighted average of the two  $\tau$  values using the area under each peak.

### **Molecular dynamics simulations**

Visual Molecular Dynamics (VMD) v.1.9.3 was used to build the dodecameric channels for Cx46 (PDB: 6MHQ) and Cx50 (PDB: 6MHY) wildtype systems for MD simulations (Humphrey et al. 1996; Myers et al. 2018). Sidechains were protonated according to neutral conditions, and the protonated HSD model was used for all histidine residues. Disulphide bonds identified in the experimental structures were enforced for both models. Amino acids corresponding to the cytoplasmic loop (CL) connecting TM2-TM3, and the C-terminal (CT) domain of Cx46 and Cx50 were not included for MD simulation, as experimental data describing the structure of these large domains (~50 residue CL and ~200 residue CT domain in Cx46 and Cx50) are missing. The introduced N- and C-terminal residues resulting from the missing CL segment (L97 and L142 in Cx46; V97 and L154 in Cx50) were neutralized. NT acetylation sites were introduced in VMD through an all-atom acetylation patch using the AutoPSF plugin, to mimic the in vivo co-translational modification identified in the native proteins (Wang & Schey, 2009; Myers et al. 2018). The prepared protein structures were submerged in a hydration shell using Solvate v.1.0.177. Water was removed from sections of the channels corresponding to transmembrane domains, based on hydrophobic character and localization of amphipol observed in experimental cryo-EM data (~20−50 Å from the centre of the channel). To mimic a cell-to-cell junction, the VMD Membrane Builder plugin was used to add two lipid bilayers to each system, containing 1-palmitoyl-2-oleoyl-sn-glycero-3-phosphocholine (POPC), with dimensions of  $152 \times 152$  Å.

The four structural models of designed variants, Cx46-R9N, Cx46-50NT, Cx50-N9R and Cx50-46NT, were also built using VMD, as follows. First, protein-only structures of the respective wildtype models were mutated, as per the sequence differences of the NT domain (defined as residues 2–19) for the NT domain

chimeras or just the 9th residue for the point variants, using VMD's *mutator* plugin (Humphrey *et al.* 1996). The variant models were then merged with the lipid bilayers created for their respective wildtype models, described above, using VMD's *mergestructs* plugin. Lipids which overlapped with the protein models were then removed. Each model was then placed in a water box with dimensions  $150 \times 150 \times 180$  Å using VMD's *solvate* plugin. The models were neutralized using the Autoionize plugin, then 150 mM KCl and 150 mM NaCl were added to the solvent areas corresponding to intracellular and extracellular regions of the simulation box, respectively.

GPU-accelerated Nanoscale Molecular Dynamics v.2.13 (Phillips et al. 2005) was used for all classical MD simulations, using the CHARMM36 force field (Huang & MacKerell, 2013) for all atoms and TIP3P explicit model for water. Each model was prepared following the same minimization and equilibration protocol, as follows. First, the lipid tails were allowed to minimize with all other atoms fixed for 1 ns using a 1 fs timestep, allowing the acyl chains to 'melt' with constant volume at a temperature of 300 K (NVT). All subsequent simulations were performed using the Langevin piston Nose-Hoover method for pressure control (NPT). Next, the entire system, including lipids, solvent and ions, was allowed to minimize with the protein harmonically constrained (1 kcal/mol), for 1 ns using a 1 fs timestep. A third 1 ns minimization step was then applied, in which the system was free to minimize with a harmonic constraint applied only to the protein backbone (1 kcal/mol), to ensure stable quaternary structure while sidechains relax in their local environment. The entire system was then released from all constraints and subject to all-atom equilibration using a Langevin thermostat (damping coefficient of 1 ps<sup>-1</sup>), with a constant temperature of 310 K and constant pressure of 1 atm, using a 2 fs timestep for 30 ns. Periodic boundary conditions were used to allow for the particle mesh Ewald calculation of electrostatics. Finally, all models were simulated for a total of 100 ns of production, using four 25 ns replicas to facilitate statistical analysis. Each replica started from the end of 30 ns equilibration with velocities reinitialized, using a 2 fs timestep.

Root mean squared deviations (r.m.s.d.), comparing the backbone conformations of MD simulation to the original pre-equilibrated starting structures, and root mean square fluctuations (r.m.s.f.) comparing the amplitudes of backbone fluctuations during MD simulation, were calculated using VMD. All six GJ models approached a steady r.m.s.d. during the first 30 ns of the equilibration phase and maintained stability during all production runs (Fig. 1*C* and *D*).

Population distribution functions were constructed by monitoring the distance between these residues at the 9th and 12th position in adjacent ( $i \rightarrow i+1$ ) subunits (in the clockwise direction when viewed from the

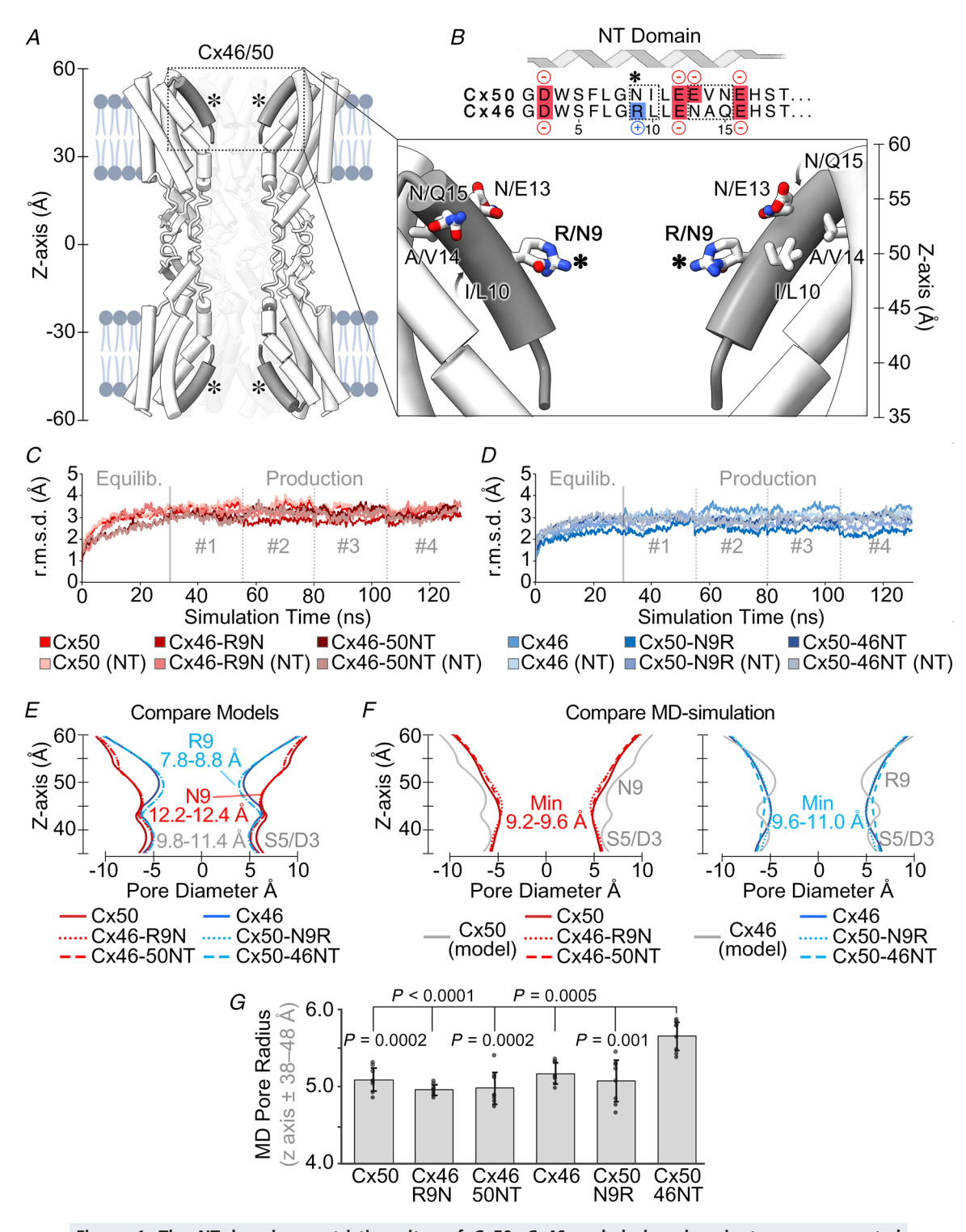


Figure 1. The NT-domain constriction sites of Cx50, Cx46 and designed variants are augmented following MD equilibration  $\frac{1}{2}$ 

A, cut-away view of Cx46/50 GJ channel shown as tube representation with the NT domain in grey. Inset: a zoom view of the NT domain with residue sidechains displayed at sites of genetic variability between Cx50 and Cx46, respectively. \*Location of residue 9 (arginine in Cx46 and asparagine in Cx50). B, primary sequence alignment of the Cx50 and Cx46 NT domain (residues 2–19). Negatively charged residues are coloured in red, positively charged residues are indicated in blue. Sites of variation between the two isoforms are indicated (dotted box). Met1 is not included, as this site is co-translationally removed and Gly2 is acetylated in both isoforms (Myers et al. 2018). C and D, backbone root mean squared deviation (r.m.s.d.) analysis of equilibrium (0–30 ns) and production phases

(30–130 ns) of the MD simulations, calculated with respect to the experimental starting structures, where Cx50, Cx46-R9N and Cx46-50NT (red traces) are shown in C, and Cx46, Cx50-N9R and Cx50-46NT (blue traces) are shown in D. R.m.s.d. analysis corresponding to just the N-terminal (NT) domains are shown in lighter shades. E, pore diameter analysis of cryo-EM-based structures of Cx50, Cx46 and the designed NT domain variants. F, averaged pore diameter of Cx50, Cx46 and designed NT domain variants following MD equilibration (pore profile of the Cx46 and Cx50 starting structures from C are shown for comparison in grey). G, bar graph summarizing the radius of NT constriction region (i.e. Z-axis  $\pm$  38–48 Å) following MD equilibration. Error bars represent SD (n = 8). All models equilibrated with a minimum constriction of  $\sim$ 4.6–4.9 Å around residue S5, with the exception of Cx50-46NT which displays a significantly wider pore constriction at S5 of  $\sim$ 5.5 Å (P50-WT = 0.000217, P46-R9N < 0.0001, P46-S0NT = 0.000176, P46-WT = 0.000468, P50-N9R = 0.00137).

cytoplasmic vestibule). Distances between functional groups were recorded at every tenth step of the trajectory across all four production runs, for Cx50, Cx46 and each of the variants. The points of reference used to measure the interatomic distance were chosen to capture equivalent rotameric states, as follows:  $C_{\zeta}$  for R9,  $C_{\gamma}$  for N9 and  $C_{\delta}$  for E12. Histograms (bin size = 0.1 Å) were normalized and plotted as probability density functions.

### **Energetics and analysis of ion permeation pathway**

Potentials of mean force (PMF), or the energy landscape, describing the permeation of K<sup>+</sup> and Cl<sup>-</sup> were calculated for all systems. To calculate the PMF, a Markov state model (MSM) was constructed by defining state-space as the position of an ion along the pore-axis (z-axis), which was subdivided into 3 Å bins. A transition matrix (T), which describes the time evolution of the system, was constructed from the conditional probabilities T<sub>ij</sub> of an ion ending up in state j after a given lag-time, having begun in state i. As in previous work (Myers et al. 2018), we employed a short lag-time (2 ps), ensuring the vast majority of transition probabilities occurred between nearest neighbours (i.e.  $i - 1 \longleftrightarrow i \longleftrightarrow I + 1$ ). The principle of detailed balance guarantees that any connected paring of states (e.g. neighbours only) is sufficient to determine the unique equilibrium distribution independent of lag time. Transition probabilities are estimated by counting the instances of transitions at every lag time and storing the values in a transition count matrix. The count matrix was then row-normalized to achieve an approximate transition probability matrix (T)

$$T_{i,i+1} \cong \frac{N_{i,i+1}}{N_i} \tag{2}$$

where  $N_{i,i+1}$  is the number of transitions from state (i) to state (i+1) in a lag time  $\tau=2$  ps, and  $N_i$  is the number of times an ion was found in state i. The thermodynamics underlying ionic permeation may then be extracted using the principle of detailed balance (i.e. statistical equilibrium) (Eqn 3) and Boltzmann statistics (Eqn 4).

$$P_i^{\text{eq}} T_{i,i+1} = P_{i+1}^{\text{eq}} T_{i+1,i}$$
 (3)

$$e^{\frac{-\Delta G_{i,i+1}}{RT}} = \frac{P_{i+1}^{\text{eq}}}{P_i^{\text{eq}}} = \frac{T_{i, i+1}}{T_{i+1, i}}$$
(4)

PMF (i) = 
$$\sum_{n=1}^{i-1} \Delta G_{n,n+1} = -\sum_{n=1}^{i-1} RT \ln \left( \frac{T_{n,n+1}}{T_{n+1,n}} \right)$$
 (5)

Here,  $P_i^{eq}$  is the probability that an ion will be in each respective bin once equilibrium is achieved,  $\Delta G_{i,i+1}$  is the free energy difference between the two states, R is the ideal gas constant (1.986 cal/mol/K), and T is temperature (310 K) (Eqn 5). Values from the PMF were mapped to the z-axis, interpolated and smoothed using a b-spline. Final PMFs were symmetrized around the centre of the channel and adjusted such that the bulk regions were at zero. To enable sufficient sampling of Cl<sup>-</sup> ions in the channel, a distributed seeding approach was implemented where an individual Cl<sup>-</sup> is randomly placed within the channel, followed by short 10 ns simulations, and repeated until sufficient sampling for the MSM is achieved. Further explanation and a detailed justification of the distributed seeding approach, and PMF calculation can be found in Myers et al. (2018).

Coulombic surface potentials were calculated using the Adaptive Poisson Boltzmann Solver (APBS) (Jurrus et al. 2018) within Chimera (Pettersen et al. 2004), using standard settings. Pore profile analysis of the radius at each point along the pore-axis (Z-axis) was calculated using the program HOLE (Smart et al. 1996). The calculation is done by rolling a sphere with the radius of a water molecule over the Van der Waals surface of the pore, with the beginning/end of the pore being defined as having a maximum radius of 12 Å. To assess the average pore profile of each model obtained by MD simulation, a snapshot of the protein was saved every 1000th frame (i.e. 2 ns), symmetrized, and then averaged together to provide the average pore profile.

### Statistical analysis

Data are expressed as mean  $\pm$  SD (or mean (SD)). A Kruskal-Wallis test followed by a Dunn's *post hoc* test was used to compare multiple groups of non-parametric data, as specified. One-way ANOVA was used to compare multiple groups of data with Gaussian distribution.

Statistical significance is indicated on the graphs only for biologically meaningful group comparisons. MD data are expressed as mean (SD), or  $\pm$  95% confidence interval where indicated. Statistical significance for MD data were calculated via a standard two-mean p-value test (Williams, 1991), using the mean values obtained from the symmetry halves of each system over the four production runs (n = 8). The nature of the distributed seeding protocol used to calculate Cl<sup>-</sup> PMF's precluded similar analysis, and so these data were not subjected to comparative statistical analysis and instead reported based on the average of the two symmetry halves of each system (n = 2).

#### **Results**

### Design of variants to probe channel properties of Cx46 and Cx50

The NT domains of Cx46 and Cx50 adopt an amphipathic helix that folds into the GJ pore, contributing to the cytoplasmic vestibules of the channel and differ at only five sites (Fig. 1A and B). This conformational state of the Cx46 and Cx50 NT domain is shown to be stable during multiple replicates of all-atom MD simulation (Fig. 1C) and D). Proteomics analysis on native proteins isolated from the lens indicated that Met1 is removed and the resulting NT Gly2 position is acetylated co-translationally in both isoforms (Shearer et al. 2008; Myers et al. 2018). The first difference in structure occurs at position 9, which is a positively charged arginine in Cx46 and a neutral asparagine in Cx50 (indicated by asterisk in Fig. 1A and B). In the cryo-EM based models, R9 of Cx46 restricts the pore diameter to  $\sim$ 8.8 Å and was identified as forming the main constriction site within the NT domain (Fig. 1*E*; Myers *et al.* 2018). In comparison, Cx50's diameter at this site is significantly wider in the cryo-EM-based model, at 12.4 Å (with a minimum constriction of  $\sim$ 11.4 Å located lower on the NT domain near S5/D3) (Fig. 1E). Further comparisons show the NT of Cx50 lacks any positively charged amino acids (assuming neutralizing of the N-terminal G2 position by acetylation), resulting in an overall net charge of -4, whereas the net charge on the Cx46 NT domain is -2 (Fig. 1*B*). Other differences localize to the identity of the hydrophobic positions 10 and 14, which form packing interactions with TM1/2 (Fig. 1A) and B).

Based on these structural comparisons, and previous MD studies which indicated that Cx46 introduces a significant energetic barrier to K<sup>+</sup> permeation as compared to Cx50 that is localized to the NT domain (Myers *et al.* 2018), we constructed four models designed to probe the mechanistic and functional role of the NT-domain and the residue identity at the 9th position for comparative all-atom equilibrium MD simulation and electrophysiology studies in GJ-deficient N2A cells.

To facilitate the most direct comparisons, all models and constructs used for experimental characterization were based on the sheep Cx46 and Cx50 structures, and correspond to NT domain swapped chimeras (Cx46-50NT and Cx50-46NT), and single point variants at the 9th residue (Cx46-R9N and Cx50-N9R). These models and/or constructs were then used to test the hypothesis that the NT domain and/or position-9 are important in defining key differences in channel properties that exist between the closely related Cx46 and Cx50 GJs.

## Position 9 does not form the primary NT domain constriction site in Cx46, Cx50 or their variants during MD simulation

Constructed models of NT domain swapped chimeras and single point variants at position-9 of Cx46 and Cx50 were built by *in silico* mutation, and the NT position (G2 in all models) was acetylated (Myers *et al.* 2018). Pore profile analysis, using the program HOLE (Smart *et al.* 1996), show the resulting models produced pore constriction sites as expected based on the identity of position-9 (Fig. 1*E*), with some differences resulting from the precise conformation selected by the modelling program for the position-9 variants.

Following all-atom MD equilibration in explicit water, the NT domains of all models appeared well behaved and maintained alpha-helical secondary structure; however, the pore profiles of all constructs were modified within the NT domains, as compared to their starting structures, primarily through reorientation of pore-lining sidechain residues (Fig. 1C-F). In contrast to the experimental starting models, the ensemble of structures obtained by MD displayed averaged steric landscapes that were all very similar to each other (Fig. 1F). Cx50, Cx46-50NT and Cx46-R9N all converged to a similar profile, with a primary constriction site diameter of  $\sim$ 9.2 (0.3) – 9.6 (0.4) Å that is substantially smaller than the experimental model of Cx50, and defined primarily by S5/D3 (Z-axis approximately  $\pm$  40 Å) (Fig. 1F, red traces). In comparison, Cx46, Cx50-46NT and Cx50-N9R all converged to a similar profile that is larger than the experimental model of Cx46, ranging from  $\sim$ 9.7 (0.3) Å for Cx46 and Cx50-N9R to  $\sim$ 10.9 (0.4) Å for Cx50-46NT (Fig. 1F, blue traces). Notably, the MD equilibrated radius of Cx50-46NT is significantly wider than all other models (P = 0.00468 - < 0.0001) (Fig. 1F and G), which is of potential interest to channel function and discussed in further detail in the following sections.

In contrast to the cryo-EM-based models, in all related MD models, the R9 position is no longer contributing as the primary constriction site. Upon closer inspection, it is observed that R9 adopts a dynamic exchange of

conformational states during MD simulation of Cx46, Cx50-46NT and Cx50-N9R, that reorients the sidechain away from the pore permeation pathway (Fig. 2). These conformations include the formation of a salt bridge between the positively charged R9 sidechain and the negatively charged E12 position (heavy atom distance = 2.6 Å) of a neighbouring subunit at the (i+1) position (Fig. 2B and C), which is a conserved site in all models (see Fig. 1B). Amongst the three variants containing an arginine at position-9, this interaction accounts for  $\sim$ 30–50% of the conformational states observed by MD (Fig. 2E). An alternative, and

less populated, conformational state is also observed, where R9 forms an optimal  $\pi$ - $\pi$  stacking interaction with guanidinium group of a neighbouring R9 (planar distance = 3.5 Å) from an adjacent subunit at the i+1 position (Fig. 2*B* and *D*) (Vernon *et al.* 2018). This state appears to be further stabilized by salt bridge formation between R9 and E12 of the same subunit (Fig. 2*B* and *D*), or between neighbouring subunits (similar to the state shown in Fig. 2*C*). This conformation was observed in  $\sim$ 5-10% of the total conformational states observed by MD (Fig. 2*F*). In all cases, these bridging interactions effectively withdraw the large R9 sidechain away from the

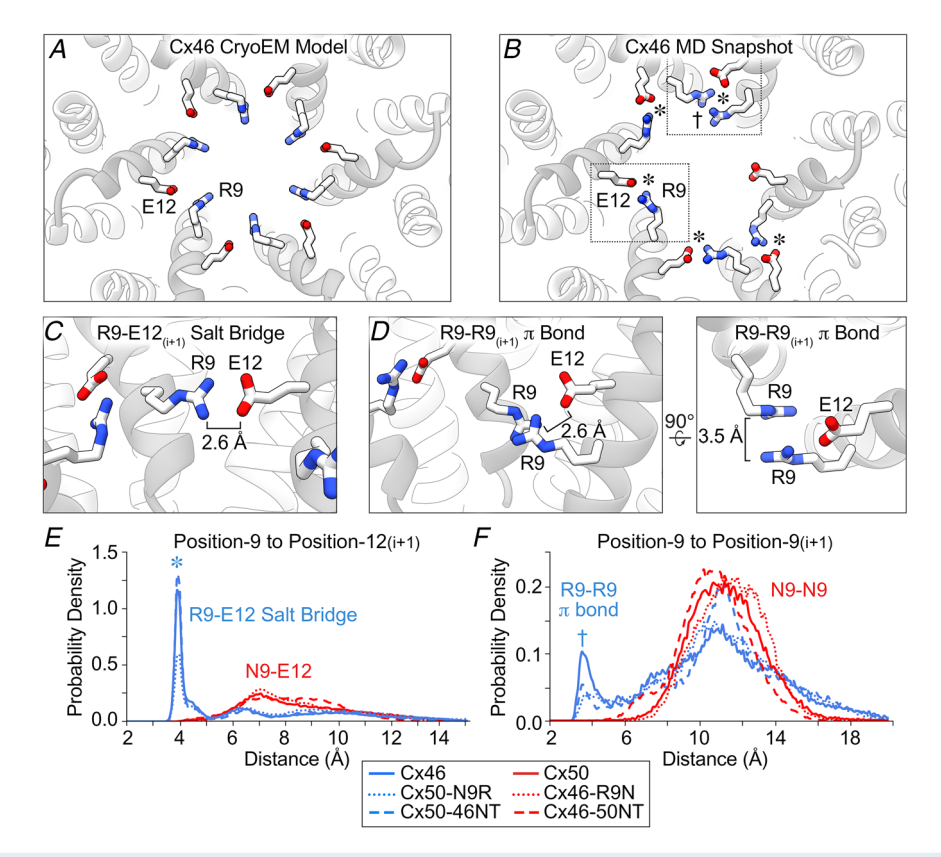


Figure 2. Arginine-9 of Cx46 and designed variants adopts a dynamic ensemble of stable conformational states that prevent pore constriction

permeation pathway and stabilize R9 against the lumen of the channel. Equivalent interactions were not observed in variants where position-9 is occupied by asparagine, with N9 appearing to adopt more random (fluctuating) conformational states (Fig. 2*E* and *F*).

Importantly, the reorganization and dynamic behaviour of the NT domain sidechain conformations observed during MD simulation are consistent with the experimental cryo-EM data that were used to build the atomic starting models. This is because, in contrast to the hydrophobic NT anchoring sites, the conformational states of the pore-lining NT domain residues, especially position-9, were not well defined by experimental cryo-EM density (presumably reflecting the specimen heterogeneity and/or intrinsic dynamic behaviour of these residues) (Myers *et al.* 2018).

## Position 9 defines a key energetic difference in K<sup>+</sup> ion permeation in Cx50 and Cx46, and their mutational variants

Given the similarities between Cx50 and Cx46 pore constriction sites observed by MD, we next sought to understand how postion-9 and the NT domain may contribute to differences in their respective energetic barriers to ion permeation by evaluating the PMF for Cl<sup>-</sup> and K<sup>+</sup>, which can be extracted from the MD data to describe the free-energy landscapes of these ions along the permeation pathway (i.e. the Z-axis) (Fig. 3). Note that inspection of the Coulombic surface of the Cx50 starting model shows that this isoform lacks any positive charge within the pore, when the NT is acetylated (Fig. 3A). In contrast, Cx46 possesses a prominent ring of positive Coulomb potential, belonging to R9, that lines the cytoplasmic vestibules at both ends of the channel (Z-axis approximately  $\pm$  50 Å) (Fig. 3A). The Coulombic surface potentials of the resulting mutation models are similar to their wildtype counterparts based on the presence or absence of an arginine at the 9th position (data not shown).

Consistent with their Coulombic surface properties, the MD-derived PMFs for Cl<sup>-</sup> showed a large peak energetic barrier,  $\Delta G_{\text{Cl}}$ . ~5.1 kcal/mol for both Cx50 and Cx46 (defined as the difference between bulk solvent and peak PMF barrier to Cl<sup>-</sup>), which is at least twice as high as the peak energetic barriers to K<sup>+</sup> (Fig. 3*B*). The primary energetic barrier to both Cl<sup>-</sup> and K<sup>+</sup> are established within the NT-domain region of the channels, and are consistent with this domain acting as the selectivity filter and with the displayed preference for cations that has been previously demonstrated experimentally for both Cx50 and Cx46 (Trexler *et al.* 1996; Srinivas *et al.* 1999; Sakai *et al.* 2003; Tong *et al.* 2014). We have therefore focused the following comparative analysis to the energetic differences

between Cx50, Cx46 and the designed variants to their energetics of K<sup>+</sup> (the major permeant ion).

The most distinct energetic differences between Cx50 and Cx46 correspond to the region of the NT domain that aligns with position-9, where Cx46 has a peak energy barrier to K<sup>+</sup> of ~2.24 (0.24) kcal/mol and Cx50 has a peak barrier of ~1.42 (0.08) kcal/mol, values that agree with our previous study using slightly modified simulation conditions (see Methods) (Myers *et al.* 2018). The difference in peak K<sup>+</sup> PMF barriers in these two models ( $\Delta\Delta G_{\rm K+} = 0.82$  kcal/mol; P < 0.0001) is expected to be primarily due to the positive charge characteristics of R9, and not local differences in channel diameter (as described in the previous section).

The K<sup>+</sup> ion PMF profiles for the designed variants show that replacing the entire NT domain of Cx46 with that of Cx50 (Cx46-50NT) or the 9th residue (Cx46-R9N) substantially reduced/eliminated the differences of NT domain energy barriers, as compared to Cx46  $(\Delta \Delta G_{K+} = 0.03-0.2 \text{ kcal/mol})$ , by effectively reducing the peak barrier around the 9th position (Fig. 3C and E). Likewise, replacing the entire NT domain of Cx50 with that of Cx46 (Cx50-46NT) or the 9th residue (Cx50-N9R) also reduced the energy difference between Cx46 and Cx50 ( $\Delta\Delta G_{\text{K+}}=0.04$ –0.4 kcal/mol), but this time by increasing the peak barrier to a similar level of Cx46 (Fig. 3D and E). Notably, although the K<sup>+</sup> energy barrier obtained for Cx50-46NT ( $\Delta G_{K+} = 1.82$ (0.17) kcal/mol) is significantly larger than wildtype Cx50 (P = 0.000392), it remains lower than that of Cx46(P = 0.00481) (Fig. 3E). This difference is proposed to reflect the larger pore diameter of this model, resulting in a less constrictive environment for ion permeation (see Fig. 1F and G). Taken together, these data confirm that the primary difference in K<sup>+</sup> energy barriers between Cx46 and Cx50 is due to the placement of a positively charged arginine at the 9th position, and led to the hypothesis that swapping these sites/domains would effectively convert the ion conductance properties of these channels, which was tested by the experiments described in the following sections.

# Cx46-50NT forms non-functional GJ channels, and is reflected by steric clash and NT-domain instability observed by MD-simulation

To integrate the results of our structural models and MD studies to GJ channel properties, we generated sheep Cx46, Cx50, the NT domain swapped chimeras (Cx46-50NT and Cx50-46NT), and point variants at the 9th residue (Cx46-R9N and Cx50-N9R) and expressed each of them in GJ-deficient N2A cells for functional characterization. N2A cells were transfected with expression vectors containing one of our designed

constructs and an untagged GFP (e.g. Cx46-IRES-GFP, Cx46-R9N-IRES-GFP, Cx46-50NT-IRES-GFP, Cx50-IRES-GFP, Cx50-N9R-IRES-GFP or Cx50-46NT-IRES-GFP) (Fig. 1A and B). Cell pairs with positive expression of GFP were voltage clamped using dual whole cell patch clamp technique. Approximately half of the cell pairs expressing Cx46 or Cx50 showed junctional currents ( $I_j$ s) in response to a  $V_j$  pulse (Fig. 4A and B), indicating successful formation of functional GJs.

Cell pairs expressing the chimera, Cx50-46NT or one of the point variants (Cx46-R9N and Cx50-N9R) were also frequently coupled with similar coupling percentages as those of wildtype lens connexins (Fig. 4A and B). However, none of the cell pairs expressing Cx46-50NT showed any  $I_j$ s in six independent experiments (Fig. 4A and B). The average coupling conductance ( $G_j$ ) for each expressed construct was calculated from the GFP+ cell pairs and no significant differences were observed among

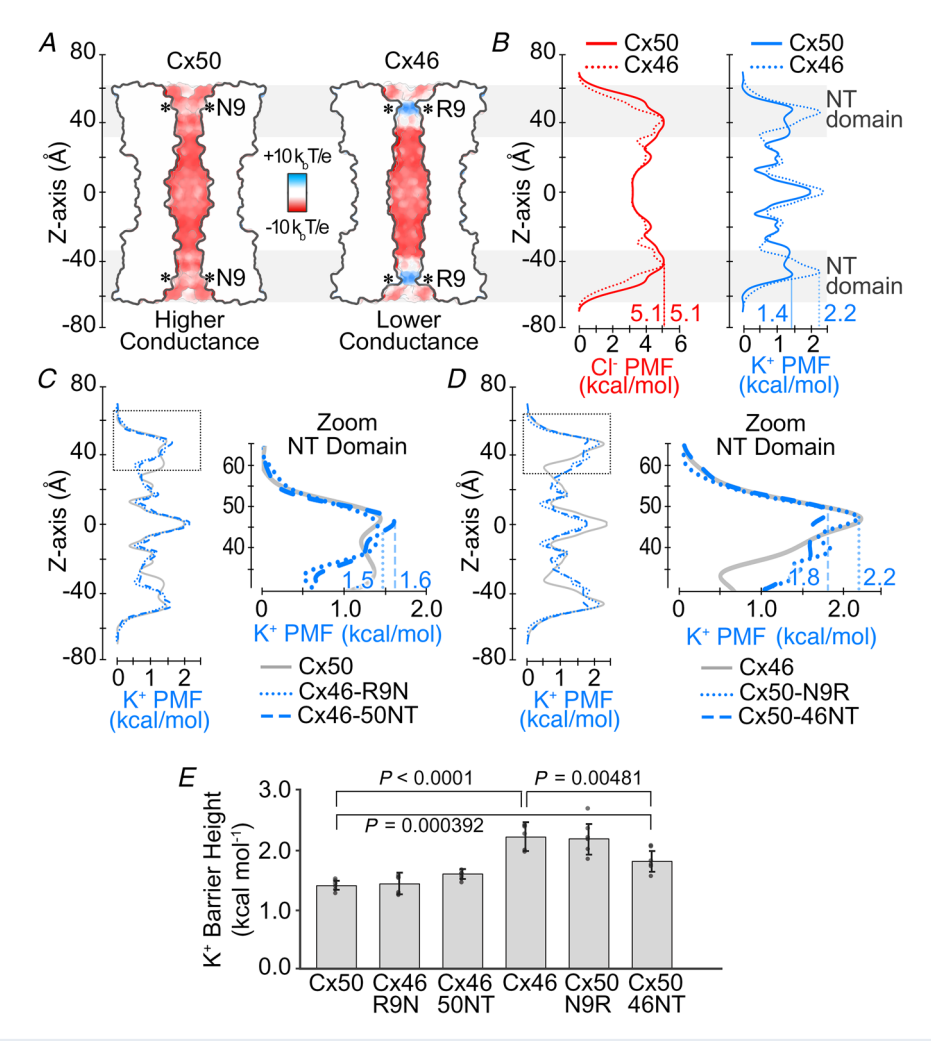


Figure 3. Electrostatics and energetics of the ion permeation pathways of Cx50, Cx46 and designed NT domain variants

A, cut-away surface representation of Cx50 and Cx46, coloured according to Coulombic potential (red, negative; white, neutral; blue, positive). T, temperature; k, Boltzmann constant; e, charge of an electron. B, potential of mean force (PMF) describing the free-energy landscape ( $\Delta G$ ) experienced by Cl<sup>-</sup> ions (red traces) and K<sup>+</sup> ions (blue traces) permeating the channel pore of Cx50 and Cx46, as compared to the bulk solvent. C, PMFs of K<sup>+</sup> ions for designed variants Cx46-R9N and Cx46-50NT, with PMF for Cx50 displayed for comparison (grey trace). Inset: zoom view of K<sup>+</sup> PMFs corresponding to the NT domain in C (dotted box region). D, PMFs of K<sup>+</sup> ions for designed variants Cx50-N9R and Cx50-46NT, with corresponding PMF for Cx46 displayed for comparison (grey trace). Inset: zoom view of K<sup>+</sup> PMFs corresponding to the NT domain in E (dotted box region). PMFs were symmetrized along the Z-axis, and peak energetic barriers identified within the NT domains are indicated. Asterisk (\*) in E in E in E indicates the location of position 9. Grey box in E in E indicate the region of the NT domain. E is a graph showing the peak energy barrier to E permeation for all variants. Error bars represents SD (E = 8). Cx50 and Cx46 display significant differences (E < 0.0001), and both Cx50 and Cx46 are significantly different from Cx50-46NT (E = 0.000392 and 0.00481, respectively).

different constructs with the exception of Cx46-50NT (Fig. 4C).

To test if the failure of Cx46-50NT to form functional GJs was due to impairment in the localization of this chimera, we used GFP fusion tagged at the carboxyl terminus of Cx46-50NT. As shown in Fig. 4D and E, Cx46-50NT-GFP was localized in intracellular compartments and displayed GJ plaque-like clusters at the cell-cell interfaces with a higher percentage than that of Cx46-GFP, suggesting that it is unlikely due to abnormal localization of this chimera for its failure in forming functional GJs. For comparison, Cx46-R9N-GFP showed a similar percentage of forming GJ plaques as that of Cx46-GFP (Fig. 4D and E).

To gain insight into the molecular basis for the loss of GJ channel function in the Cx46-50NT chimera, we further interrogated the MD simulation data for this construct. Notably, the dynamic behaviour of the NT domain in this construct is significantly higher compared to the wildtype Cx46 model, as assessed by the backbone r.m.s.f., which describes the amplitude of backbone dynamics (Fig. 4F; P = 0.000273 over residues 3–20). In comparison, the NT r.m.s.f. values of wildtype Cx50 were not significantly different from the Cx50-46NT model. The reason for the decreased stability of the NT domain in the Cx46-50NT chimera is suspected to be the introduced changes in hydrophobic anchoring residues that dock against the TM domains (Fig. 1A and B). Specifically, placement of

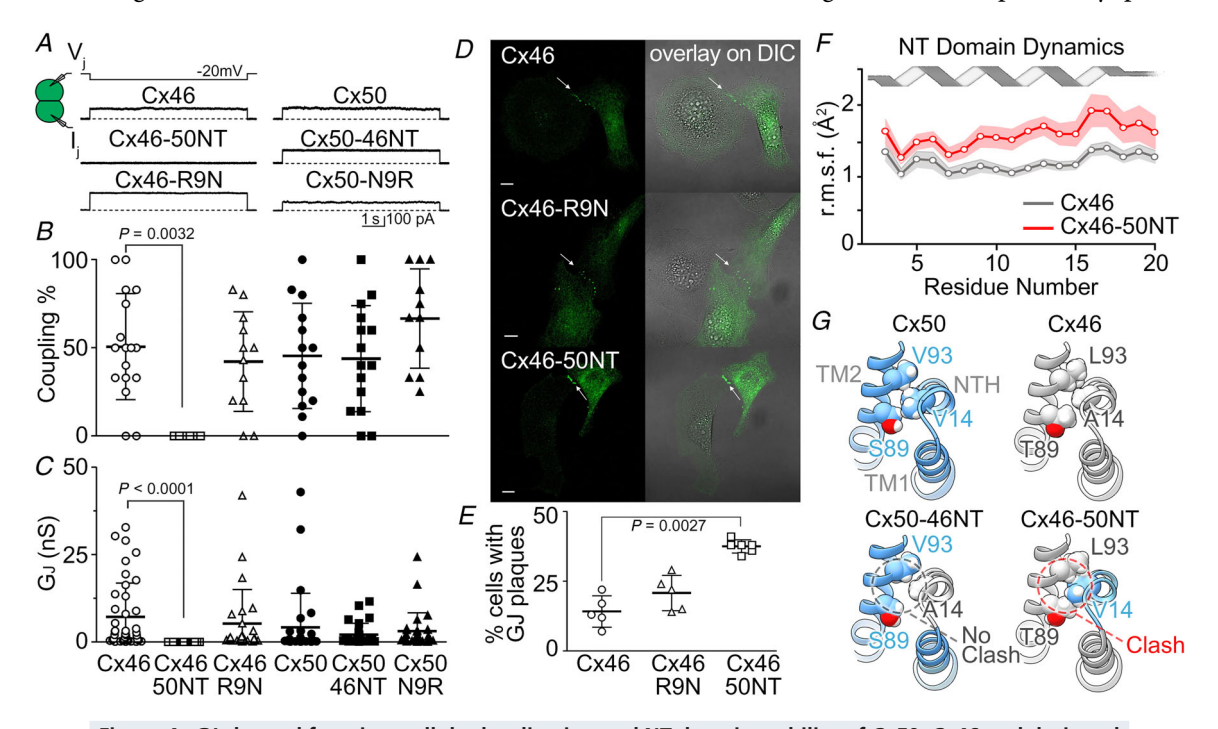


Figure 4. GJ channel function, cellular localization and NT domain stability of Cx50, Cx46 and designed NT domain variants

A, dual whole-cell patch clamp technique was used to measure junctional current  $(I_i)$  in N2A cell pairs expressing GFP-tagged constructs of sheep Cx50, Cx46 and NT domain variants (Cx50-N9R, Cx50-46NT, Cx46-R9N and Cx46-50NT) in response to a -20 mV  $V_i$  pulse. B, bar graph showing the average coupling percentages of cell pairs expressing homotypic sheep Cx50, Cx46 and designed NT domain variants. One-way ANOVA followed by Newman-Keuls post hoc test was used compare each of the variants with their respective controls. Cx46-50NT showed no coupling, which was significantly different from that of wildtype Cx46 (P = 0.0032). The number of transfections is indicated. C, bar graph showing the average coupling conductance  $(G_i)$  of GFP+ cell pairs. Kruskal-Wallis followed by Dunn's post hoc test was used to compare each of the variants with their respective controls. The total number of cell pairs is indicated. D, cell imaging of GFP-tagged Cx46, Cx46-R9N and Cx46-50NT expressed in connexin-deficient HeLa cells. GJ plaque-like structures (arrows) similar to that of Cx46-GFP (upper panels) are identified for both Cx46-R9N and Cx46-50NT variants. GFP fluorescent signals are superimposed onto DIC images to show the localization of these fluorescent signals (panels on the right). Scale bars = 10  $\mu$ m. E, bar graph showing the percentage of cells expressing each of the constructs displaying GJ plague-like structures at the cell-cell interfaces. Note that the Cx46-50NT showed a significantly higher percentage of GJ plaque-like structures (P = 0.0027). F, line graph showing NT domain dynamics obtained by MD simulation, as assessed by the backbone root mean square fluctuation (r.m.s.f.) for Cx46 (grey trace) and Cx46-50NT (red trace). Shaded boundaries indicate the 95% confidence intervals (n = 12). Residues 3–20 show a significant difference between these models (P = 0.000273). G, structural comparison of hydrophobic packing interactions involving residue 14 on the NT domain and residues 89 and 93 on TM2 of Cx50, Cx46 and chimeric models for Cx50-46NT and Cx46-50NT. The Cx46-50NT chimera introduces a steric clash involving bulky residues V14 and T89.

the Cx50 NT domain onto the Cx46 channel introduces an apparent steric clash between V14 and T89 (located on TM2) (Fig. 4G). In Cx50, position 89 is occupied by a small serine residue, which can accommodate a bulky V14 anchoring residue. In contrast, Cx46 appears to compensate for the smaller A14 anchoring site with a bulkier T89 residue. Of further comparison, when the Cx46 NT domain (containing the smaller A14 site) is placed onto the Cx50 channel (containing the smaller S89 site), a vacant space is introduced between the NT domain and TM2 of the Cx50-46NT chimera (Fig. 4G). This arrangement allows the NT domain to pack more closely against TM2 during MD simulation, resulting in the larger pore diameter of this construct as compared to Cx46, Cx50 and other variant models (see Fig. 1F and G). Note that the NT r.m.s.f. of this chimera was also significantly lower (i.e. more stable) as compared to the non-functional Cx46-50NT variant (P = 0.00526; over residues 3-20).

## Swapping the NT-domain or the 9th residue of Cx46 onto Cx50 alters $V_j$ gating, while $V_j$ gating of Cx46-R9N is unaffected

To investigate the effects of NT domain variants on transjunctional voltage-dependent gating ( $V_i$  gating), cell pairs forming homotypic GJs were recorded by dual whole cell patch clamp and their  $I_i$ s were measured in response to a series of  $V_i$  pulses from  $\pm 20$  to  $\pm 100$  mV (Fig. 5A). The Iis of Cx46 and Cx50 GJs both showed symmetrical  $V_i$ -dependent deactivation, with similar  $V_i$ gating properties (Fig. 5A). For both wildtype GJs,  $I_i$ s in response to  $V_i$  values in the range of  $\pm 40$  to  $\pm 100$  mV showed strong deactivation (Fig. 5A). When  $V_i$  absolute value was  $\leq$  20 mV,  $I_i$ s showed no deactivation (Fig. 5*A*). The normalized steady state conductance  $(G_{i,ss})$  was plotted as a function of  $V_i$  (Fig. 5B), which could be well fitted by a Boltzmann equation (Eqn 1) for each  $V_i$ polarity, for either Cx46 or Cx50 GJs (Fig. 5B). None of the Boltzmann fitting parameters of Cx46 and Cx50 were significantly different (Table 1).

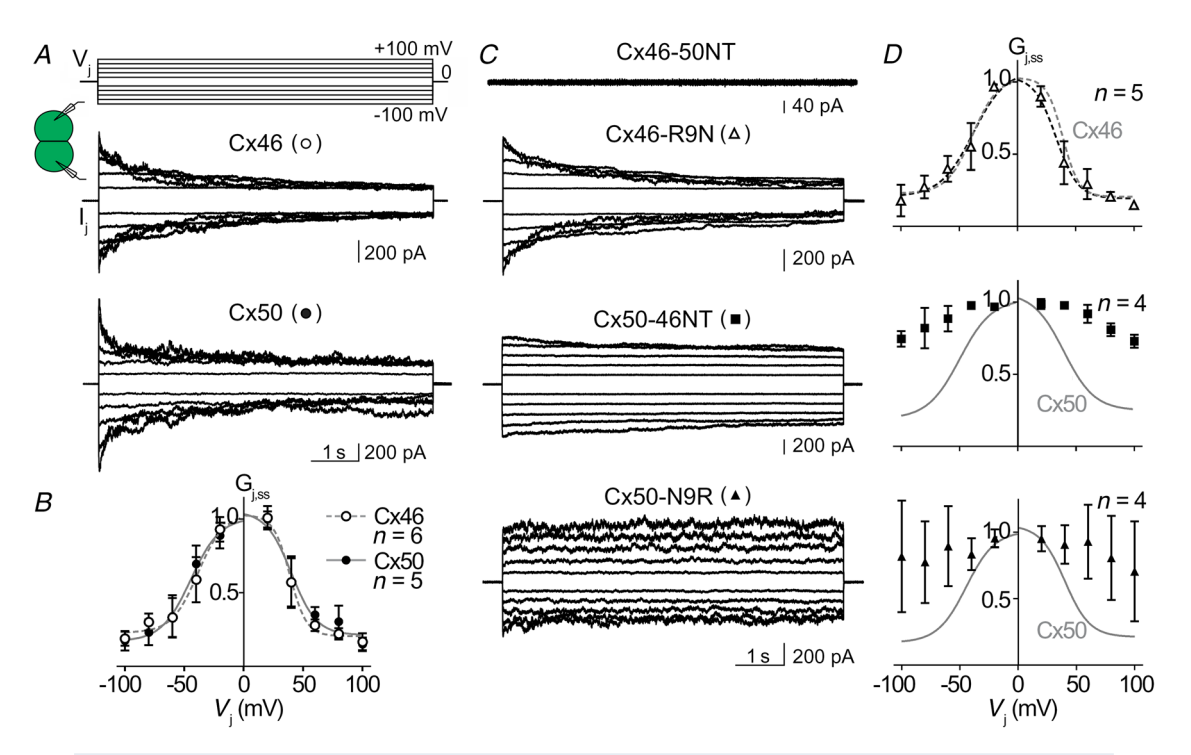


**Figure 5.**  $V_j$  gating of homotypic sheep Cx46, Cx50 and NT domain variant gap junction channels A and C, superimposed junctional currents ( $I_j$ ) recorded from cell pairs expressing homotypic sheep Cx46 or Cx50 GJs (A) and NT domain variants Cx46-50NT, Cx46-R9N and Cx50-N9R GJs (C), in response to a series of  $V_j$  pulses (shown on the top of A,  $\pm 20$  to  $\pm 100$  mV with 20 mV increment). B, normalized steady state junctional conductance,  $G_{j,ss}$ , of Cx46 (open circles) and Cx50 (filled circles) plotted as a function of  $V_j$ . Boltzmann equations (Eqn 1) were used to fit  $G_{j,ss}$ – $V_j$  plots for Cx46 (smooth dashed grey lines) and Cx50 (smooth solid grey lines) GJs. D, normalized steady-state junctional conductance,  $G_{j,ss}$ , of Cx46-R9N (open triangles), Cx50-46NT (filled squares) and Cx50-N9R (filled triangles) plotted as a function of  $V_j$ . Only the  $G_{j,ss}$ – $V_j$  plot of Cx46-R9N GJ was fitted well with Boltzmann equations (smooth dashed black lines). For comparison, the Boltzmann fitting curves of wildtype Cx46 (smooth dashed grey lines) or Cx50 GJ (smooth solid grey lines) were superimposed on the respective plot. The number of cell pairs for each construct is indicated in B and D.

14 B. Yue and others J Physiol 0.0

Table 1. Boltzmann fitting parameters for homotypic sheep Cx46, Cx50, and Cx46-R9N GJs

	$V_{ m j}$ polarity	$G_{min}$	$V_0$	А
Cx46 (n = 6)	+	$\textbf{0.21} \pm \textbf{0.06}$	$39.0 \pm 3.6$	$\textbf{0.14} \pm \textbf{0.09}$
	_	$\textbf{0.23} \pm \textbf{0.08}$	$38.6 \pm 7.0$	$0.09\pm0.05$
Cx50 (n = 5)	+	$\textbf{0.21} \pm \textbf{0.12}$	$40.1 \pm 7.1$	$0.09\pm0.05$
	_	$\textbf{0.17} \pm \textbf{0.09}$	$44.5\pm7.7$	$\textbf{0.08} \pm \textbf{0.04}$
Cx46-R9N (n = 5)	+	$\textbf{0.19} \pm \textbf{0.06}$	$\textbf{33.2} \pm \textbf{5.9}$	$0.11\pm0.06$
	_	$\textbf{0.21} \pm \textbf{0.11}$	$38.0 \pm 9.8$	$0.07\pm0.05$

Data were fitted to the Boltzmann equations (Eqn 1) and are presented as mean  $\pm$  SD;  $V_0$  are absolute values. One-way ANOVA followed by Tukey's post hoc test was used to compare Boltzmann fitting parameters of all three GJs. None of the parameters showed statistically significant differences for the same  $V_j$  polarity.

 $V_i$  gating of Cx46-50NT, Cx46-R9N, Cx50-46NT and Cx50-N9R GJs were then studied using the same  $V_i$  protocol (Fig. 5C). As shown in the Fig. 5C, Cx46-50NT was unable to form functional GJs, while Cx46-R9N, Cx50-46NT and Cx50-N9R all successfully formed functional GJs. Among these functional GJs, Cx46-R9N showed strong symmetrical deactivation when  $V_i$  values were in the range of  $\pm 40$  to  $\pm 100$  mV (Fig. 5C). The  $G_{i,ss}$ - $V_i$  plot for Cx46-R9N could be well fitted with the Boltzmann equation for each  $V_i$ polarity, which showed no significant difference from those of wildtype Cx46 GJs (Fig. 5D and Table 1). The Iis of Cx50-46NT GJs showed very weak deactivation in the tested  $V_i$  values (Fig. 5C), and the  $G_{i,ss}-V_i$  plot of these channels could not be fitted with a Boltzmann equation (Fig. 5D). Similarly,  $I_i$ s of Cx50-N9R GJ also showed no consistent deactivation in the tested  $V_i$ values (Fig. 5C), and the  $G_{j,ss}$ - $V_j$  plot also could not be fitted with a Boltzmann equation for these channels (Fig. 5D). In addition, the  $I_i$ s of Cx50-N9R showed a lot of fluctuations throughout the  $V_i$  pulse (Fig. 5C) resulting in large variations in the  $G_{i,ss}$  (Fig. 5D). Together, these data indicate that the  $V_i$ -response for variants of Cx50 (Cx50-46NT and Cx50-N9R) are more susceptible to perturbation than the Cx46 variant (Cx46-R9N). A structural basis for these differences was not entirely clear, as the millisecond-second long timescales of  $V_i$  gating are beyond the limits of traditional MD simulation (see Discussion).

### Differences in Cx50 and Cx46 GJ single-channel conductance properties are defined by the 9th residue

MD simulation studies indicated that incorporation of the positively charged arginine at the 9th position of Cx46, Cx50-N9R and Cx50-46NT introduces a significant energetic barrier to  $K^+$  ion permeation (the major permeant ion of Cx46/Cx50 GJs), as compared to Cx50 and Cx46-R9N (see Fig. 3). To investigate the functional effects of this positively charged residue we characterized the unitary conductance ( $\gamma_i$ ) of Cx50, Cx46 and the

designed NT domain variants based on single channel current  $(i_j)$  recordings at varying  $V_j$  values. In Fig. 6A, homotypic sheep Cx46 and Cx50 single channel current  $(i_j)$  traces are shown at the  $V_j$  values indicated. All point histograms and Gaussian fits were used to measure the amplitudes of  $i_j$  values for the main open state at the tested  $V_j$  values (Fig. 6B). The averaged  $i_j$  values were plotted at different  $V_j$  and a linear regression  $i_j$ – $V_j$  plot for Cx46 or Cx50 GJs was used to estimate the slope unitary channel conductance  $(\gamma_j)$  (Fig. 6C). The  $\gamma_j$  of Cx46 GJ is 166 (14) pS, whereas the  $\gamma_j$  of Cx50 GJ is 208 (14) pS.

Figure 6D shows  $i_i$  values of homotypic Cx46-R9N, Cx50-N9R and Cx50-46NT GJs at the indicated  $V_i$  values. The averaged  $i_i$  values for the main open state for each tested  $V_i$  of these variants were plotted to create an  $i_i - V_i$ plot. Linear regression of the  $i_i$ - $V_i$  plot for each variant was used to estimate slope  $\gamma_i$  (Fig. 6E). Cx46-R9N GJs showed a significant increase in slope  $\gamma_i$  (261 (23) pS) from that of wildtype Cx46 GJ (Fig. 6E). Conversely, Cx50-N9R GJs displayed a significantly decreased slope  $\gamma_i$  (116 (29) pS) than that of wildtype Cx50 GJ (Fig. 6E). Replacing the NT domain of Cx50 with that of Cx46, Cx50-46NT, also resulted in a pronounced drop in slope  $\gamma_i$  (119 (13) pS). The slope single channel conductance values of all tested variants were plotted as a bar graph for direct comparison (Fig. 6*F*). These effects are qualitatively consistent with the predicted results obtained by MD, but there was a surprisingly higher degree of effect of the placement/removal of R9 leading to channel variants with correspondingly higher or lower unitary conductance, as compared to wildtype channels.

# Cx50-46NT forms GJ channels with an extremely stable open state, while Cx50-N9R open state becomes destabilized

Another surprising result revealed by single channel recordings was the effects on the open state probability of the variant GJs. As shown in Fig. 6D, the  $i_j$  values of Cx50-46NT were virtually in the fully open state (or

probability of open,  $P_{\rm open} \approx 1$ ) at all  $V_{\rm j}$  values except at 100 mV, whereas  $i_{\rm j}$  values of Cx50-N9R show a much lower  $P_{\rm open}$  at all tested  $V_{\rm j}$  values ( $P_{\rm open}$  in the range 0.11–0.22). The  $i_{\rm j}$  values of both Cx50-46NT and Cx50-N9R showed little change in  $P_{\rm open}$  in the tested  $V_{\rm j}$  values (data not shown).

Upon close inspection of the  $i_j$  of Cx46, Cx50 and their variants, we found that the open dwell times were different among different GJs. To quantify the open dwell time for each of these GJs, the  $i_j$  values of these GJs were further analysed to obtain an open dwell time for each open event (Fig. 7A). At a  $V_i$  of -60 mV, a limited

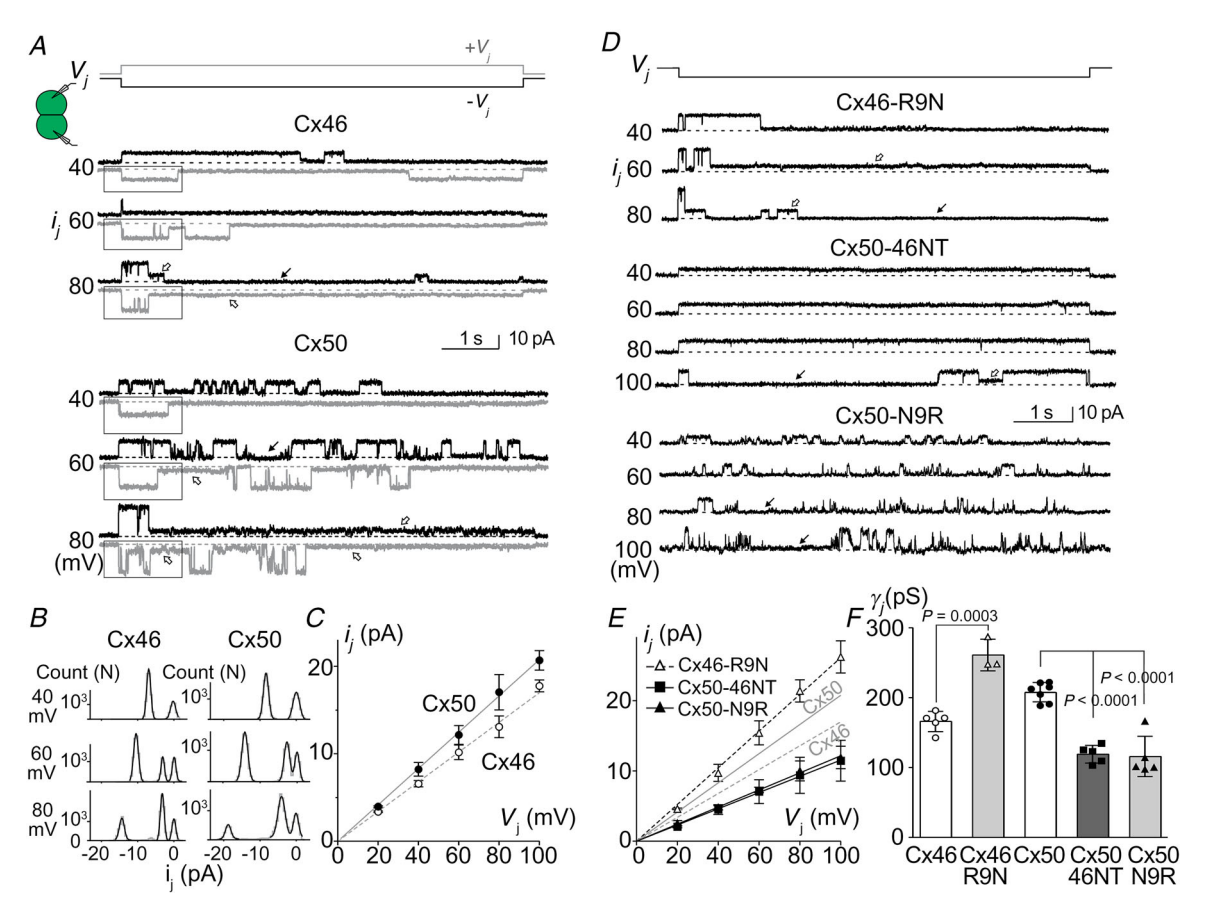


Figure 6. Single channel properties of homotypic sheep Cx46, Cx50 and NT-domain variant GJs

A, single channel currents  $(i_i)$  recorded from a cell pair expressing wildtype sheep Cx46 (top set) or Cx50 (bottom set) at the indicated  $V_i$ . Positive  $V_i$  ( $+V_i$ ) or negative  $V_i$  ( $-V_i$ ) induced  $I_i$  values are shown in grey or black, respectively. Both GJs showed a fully open state at the beginning of  $V_i$  pulses and transitions to either subconductance (open arrows) or fully closed state (solid arrows). Note that more than one subconductance state could be identified at  $\pm$ 80 mV  $V_i$ . B, all point histogram and Gaussian fits were used to estimate the  $i_i$  amplitude at the main open state for both  $V_i$  polarity. A selected section as shown in A was used to generate the all point histogram. The main conductance state and in some cases a subconductance state could be identified at different  $V_i$  values and averaged from both  $V_i$  polarities.  $C_i$ ,  $i_i$  amplitudes of the main open state were plotted at each tested  $V_i$ . The slope of the linear regression lines in the  $i_i$ – $V_i$  plot represent the slope unitary channel conductance ( $\gamma_i$ ). For Cx46 GJ, the slope  $\gamma_i = 166 (14) \text{ pS} (n = 5) \text{ and for Cx50, the slope } \gamma_i = 208 (14) \text{ pS} (n = 7). D, \text{ single channel currents } (i_i) \text{ recorded}$ from cell pairs expressing sheep Cx46-R9N, Cx50-N9R or Cx50-46NT at the indicated  $V_i$  values. The  $i_i$  values of Cx46-R9N showed a main open state at the beginning of the V<sub>i</sub> pulses and transitioned into subconductance state (open arrows) or fully closed state (solid arrow). The  $i_1$  values of Cx50-46NT preferentially reside at the fully open state at most tested  $V_i$  values (-40 to -80 mV) and transition to the fully closed state (solid arrow) or to a subconductance state at -100 mV  $V_i$ . The  $i_i$  values of Cx50-N9R showed multiple open events with frequent transitions to the fully closed state (solid arrows). E, amplitude of  $i_i$  (the same way as described in B) for the main open state at each tested  $V_j$  was plotted against  $V_i$  and analysed as described for C. The solid and dashed grey lines represent the slope  $\gamma_i$  values of Cx50 and Cx46 respectively. The slope  $\gamma_i$  of Cx46-R9N is 261 (23) pS (n = 3), Cx50-N9R  $\gamma_i$  is 116 (29) pS (n = 5) and Cx50-46NT  $\gamma_i$  is 119 (13) pS (n = 5). F, bar graph summarizing the slope  $\gamma_i$  values of all tested variants. The  $\gamma_i$  of Cx46-R9N was significantly higher than that of Cx46 and the  $\gamma_i$  values of Cx50-46NT and Cx50-N9R were significantly lower than that of Cx50 (one-way ANOVA followed by Tukey's post hoc test for biologically meaningful groups). The total number of cell pairs for each variant is shown.

number of open events (transitions from closed to open and return to the closed state) could be identified for Cx50-46NT during a 7 s  $V_j$  pulse. A few open events for Cx46 and Cx46-R9N GJs and many more open events for Cx50 and Cx50-N9R GJs were detected at the same  $V_j$  (Fig. 7*A*). The open dwell time for all events was averaged for each variant GJ (Fig. 7*b*). In most of the tested  $V_j$  values, the rank of the open dwell time from long to short is in the following order: Cx50-46NT > Cx46 > Cx50 > Cx46-R9N > Cx50-N9R GJs (Fig. 7*B*).

It is interesting to note that open event frequency was much higher for both Cx50 and Cx50-N9R GJs and both GJs showed two types of openings, short (labelled by asterisks) and long (labelled by arrows) opening events (Fig. 7A). Histograms of open dwell time were generated for both of these GJs (Fig. 7C) and each could be fitted with two-exponential components. Cx50 showed short (2 ms) and long (102 ms) open events at  $V_j = 60$  mV with a higher prevalence of the long open events (63%) (Fig. 7C). At  $V_j$  of 80 mV, the average of long open events became

shorter (90 ms) with slightly lower percentage (56%), while the average of the short open events was 3.9 ms with an increased percentage (44%). The weighted averages of time constants ( $\tau_{\rm mean}$ ) for these two  $V_{\rm j}$  values were also calculated (Fig. 7C). Upon mutating the 9th residue to arginine (Cx50-N9R) the long open events became much shorter (26 ms and 31 ms) with reduced percentages (24% and 20%), respectively for  $V_{\rm j}$  values of 60 and 80 mV. The Cx50-N9R  $\tau_{\rm mean}$  value was much lower than that of Cx50. Together, these results suggest that the identity of the 9th residues, in addition to other structural differences within the NT domains of these variants, significantly influences the open state stability of these GJs (see Discussion).

### **Discussion**

In this study, structural modelling and MD simulations were conducted in combination with macroscopic and single channel electrophysiology studies to investigate the

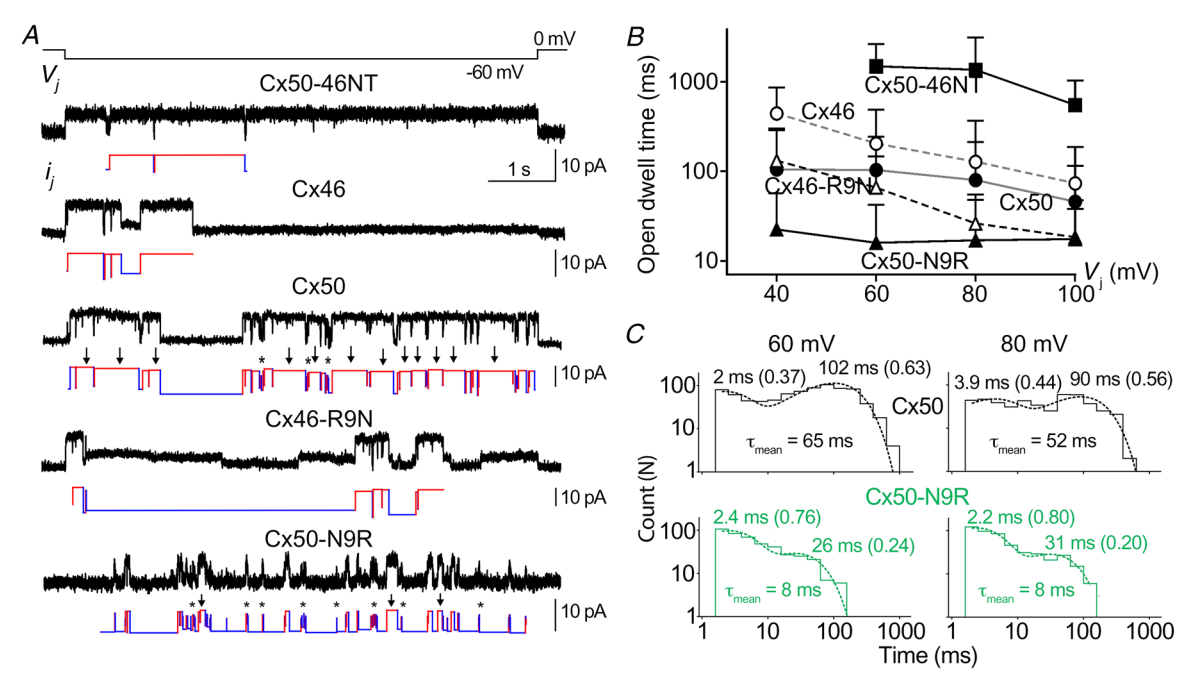


Figure 7. Single channel open state dwell times of Cx50, Cx46 and NT domain variants A,  $i_j$ s (black) and schematic single channel openings (red) and closings (blue) are shown for sheep Cx50-46NT, Cx46, Cx50, Cx46-R9N and Cx50-N9R GJs. Cx50 and Cx50-N9R GJs showed apparently short (\*) and long (arrows) open events, as well as more open events than the other GJs. Note that the first and the last open events were excluded as they probably under-represent the open dwell time (e.g. exist in the open state before or after the  $V_j$  pulse). Our  $V_j$  pulse duration (7 s) may not be sufficient to reach a true steady state and the open event properties might be slightly different from the fully stable  $i_j$  values of the studied GJs. B, averaged open dwell time for each GJ plotted at different  $V_j$  values. The number of events analysed ranged from 33 to 832 from two to seven cell pairs. Note that the open dwell time is plotted on a logarithmic scale to show large differences among these GJs. The ranking of the open dwell times of these GJs from high to low is: Cx50-46NT > Cx46 > Cx50 > Cx46-R9N > Cx50-N9R. C, open dwell time for all open events for Cx50 and Cx50-N9R were plotted in a logarithmic histogram with five bins per decade and fitted with two-exponential log components. The two time constant ( $\tau$ ) values represent the corresponding short and long open events for Cx50 (top histograms) and Cx50-N9R (bottom green histograms) are displayed, with their relative proportions in parentheses. The  $\tau_{\rm mean}$  values were calculated by taking the weighted average of the two  $\tau$  values using the area under each peak for each of these variants at a specific  $V_j$ .

mechanistic roles of NT domains in two closely related lens GJs, Cx50 and Cx46. We identified differences in structure and dynamics within the NT domains, as the key features differentiating the pore open stability and energetic barriers to ion permeation between these two isoforms (see summary of results presented in Fig. 8). In the following, we discuss the mechanistic insights gained by these results and in comparison to previous studies, as well as some unresolved discrepancies between the simulation and experimental data that point to the importance of ongoing development in our atomic-level understanding of GJ conductance,  $V_j$  gating and open state stability.

### Hydrophobic stabilization of the GJ open state

The mechanistic basis of GJ open state stability has not yet been well defined. All-atom equilibrium MD simulations conducted on wildtype channels and NT domain variants, based on cryo-EM models of Cx46 and Cx50, all maintained the novel open state conformation that is stabilized by inter- and intra-subunit hydrophobic interactions (a mechanism to anchor the NT domains in an open conformation) that are distinct from the open state originally described for Cx26 (Maeda et al. 2009; Myers et al. 2018). The importance of hydrophobic anchoring residues within the NT domain is further supported by the chimeric construct Cx46-50NT, which displayed significantly destabilized NT domain dynamics as compared to Cx46 (P = 0.000273) and this behaviour was functionally correlated with a loss of channel activity for this variant (Fig. 8 and see Fig. 4A, C). Remarkably, the non-functional Cx46-50NT GJs appeared to be able to reach the cell membrane and formed morphological GJs (see Fig. 4D and E), indicating that the loss of channel function was unlikely to be due to defects in trafficking or GJ assembly. Possible mechanistic insights to this phenotype are provided by our structural models, where this chimera introduces a specific steric clash

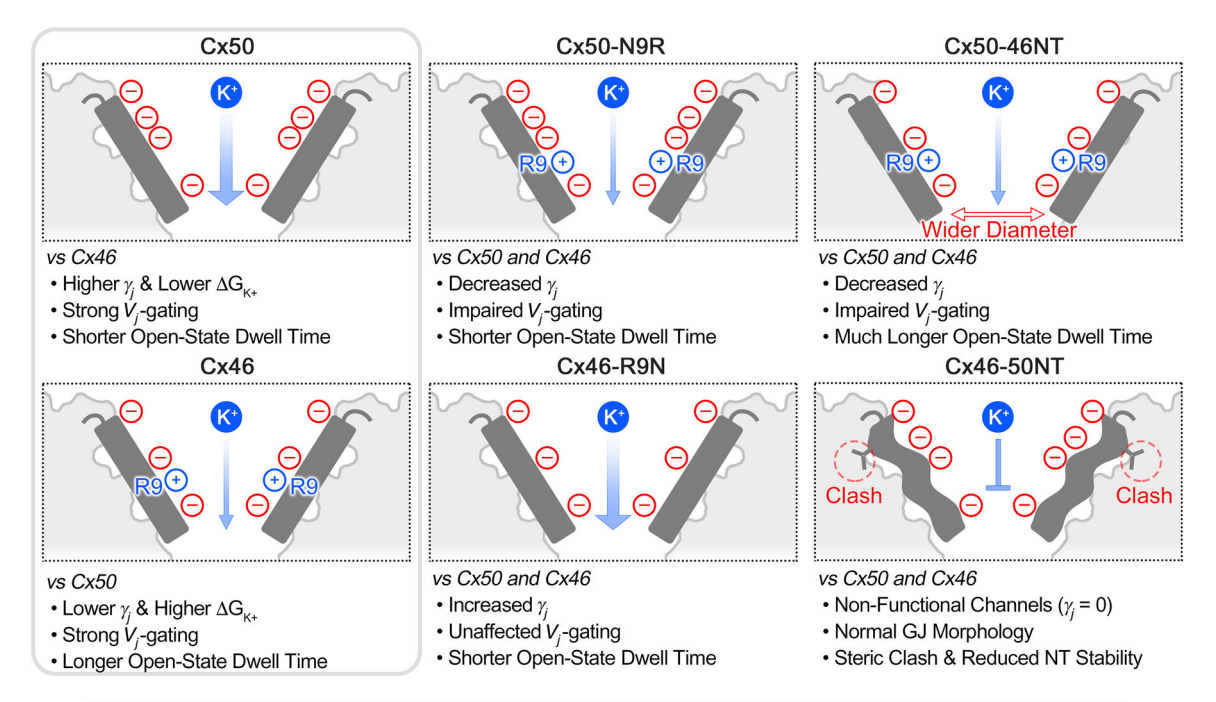


Figure 8. Overview of significant structural and functional differences between Cx50, Cx46 and NT domain variants

Cartoon illustrating the NT domain regions (shown in dark grey) and structural and/or functional differences between Cx50, Cx46 and the designed variants for this study. Locations of negatively charged residues (red circles) and positively charged R9 residue (blue circles) are indicated (see for comparison Fig. 1*B*). The relative permeabilities to the major permeant ion (K<sup>+</sup>) is indicated by the width of the blue arrow, where Cx50 displays a higher unitary conductance and lower  $\Delta G_{K+}$ , as compared to Cx46. Both wildtype GJs displayed strong  $V_j$  gating. The single point variants, Cx50-N9R and Cx46-R9N, produced channels with  $\gamma_j$  values that were augmented by adding or removing the positively charged R9 position, although these variants affected  $V_j$  gating and open state dwell times differently. The Cx50-46NT chimera displayed remarkably long open state dwell times and impaired  $V_j$  sensitivity, as compared to wildtype GJs, which correlated with a tighter packing of the NT domain to TM2, resulting in a wider pore radius compared to Cx46 or Cx50 following MD simulation. The Cx46-50NT construct formed morphological GJs, but these channels were non-functional. The loss of channel activity for this construct is proposed to be due to a steric clash that is introduced between V14 and T89 and reduced stability of the NT domain observed by MD simulation (indicated by the wavy NT domain in the illustration).

between the introduced hydrophobic residue V14 on the NT domain and T89 located on TM2 (Fig. 8 and see Fig. 4*G*). Together, these data suggest that the NT domain of Cx46-50NT becomes destabilized, probably by steric interactions involving hydrophobic anchoring sites, resulting in loss of channel function (Fig. 8). While the NT domain does not completely unfold during the relatively short time scale of our MD simulation, improper folding of the Cx50 NT domain in the context of this chimera can also not be ruled out.

In contrast to the Cx46-50NT chimera, placement of the Cx46 NT domain onto Cx50 resulted in more close hydrophobic packing (due to smaller hydrophobic residues at positions 14 and 89), which resulted in an overall wider pore diameter for this construct, as compared to wildtype and the other designed GJs (P = 0.000468 to < 0.0001). We suggest that this close packing results in a more stabilized NT domain and contributes, at least in part, to the increased open dwell time and reduced  $V_i$  gating of this GJ. Quantitative measurements of open dwell time of the Cx50-46NT GJ showed they were about 5-15 times longer than those of Cx46 and Cx50 GJs (see Fig. 7). It is interesting to note that in previous studies on switching NT domains of orthologous Cx50 and Cx46 GJs and hemichannels, the authors also showed a decrease in unitary conductance and an increased open dwell time in Cx50-46NT as compared to wildtype (Tong et al. 2004; Tong & Ebihara, 2006; Kronengold et al. 2012). Surprisingly, the hemichannel of Cx46-50NT was functional (unlike our result that sCx46-50NT was unable to form functional GJs) with a slightly higher hemichannel unitary conductance (Kronengold et al. 2012). The basis for this functional difference is not clear, as the NT domain and position 89 (the site of steric clash in our Cx50-46NT model) are conserved between sheep and rodent. However, other differences in experimental conditions that may influence NT domain stability cannot be ruled out, such as cell expression system (Xenopus oocyte versus N2A cells) and/or GJ versus hemichannel

More broadly, these results reinforce the proposal that hydrophobic anchoring sites within the NT domain play an important functional role in stabilizing the open state conformation resolved in the Cx46/50 cryo-EM structure (Myers *et al.* 2018), and probably play a similar functional role in other GJs based on conservation of hydrophobic positions found in other isoforms. This interpretation is consistent with previous studies. For example, the congenital cataract-associated L11S mutation in Cx46 has been shown to result in proper trafficking to the plasma membrane, but showed no GJ or hemichannel activity (Tong *et al.* 2013). The authors contextualized these results based on the available Cx26 structure; however, we believe that has led to misleading interpretation of this mutation

(and other previous mutational studies at these hydrophobic sites), as the hydrophobic sites in the Cx26 GJ structure are displayed toward the permeation pathway of the channel (Maeda *et al.* 2009).

We suggest the conformational state of the NT captured in Cx46/50, and proposed role of the hydrophobic residues within this domain in stabilizing the open state, are congruent with mutational studies in other isoforms as well. In Cx26, an M34T mutation associated with hereditary deafness significantly reduces channel conductance and has been proposed to disrupt the open stability of the channel via interactions with W3 in the NT domain of Cx26 (equivalent to W4 in Cx46/50) (Maeda et al. 2009; Zonta et al. 2014). The similar M34A mutation in Cx26 results in non-functional channels and has been shown structurally to disrupt the open state conformation of Cx26, inducing an apparent closed-state conformation with a plug density blocking the pore permeation pathway (Oshima et al. 2007, 2011). Notably, position L35 in Cx46/50 (equivalent to position M34 in Cx26) also interacts with W4, although the details of this interaction are different in the context of the more stabilized NT domain conformation (Myers et al. 2018). Nevertheless, mutation at this site would predict a similar disruption to the open state NT conformation. In Cx32, a series of mutations have been conducted that scan the functional effect of replacing NT domain residues with a negatively charged aspartate (Purnick et al. 2000). Remarkably, replacement of hydrophobic residues, such as W3D, L6D, L9D or L10D (equivalent to the NT hydrophobic anchoring residues 4, 7, 10 and 11 in Cx46/50), all resulted in non-functional GJs, while mutations performed at other non-hydrophobic sites produced functional channels with altered conductance/gating properties (Purnick et al. 2000).

These correlations all support the over-arching proposal that the open state stability of GJs is driven by inter- and intra-subunit hydrophobic interactions between the NT and TM1/TM2, while genetic mutations that disrupt these hydrophobic packing interactions may lead to significant destabilization of the NT domain, resulting in non-functional channel formation with pathological consequences of disease. We note, however, that the molecular details involved in stabilizing the open-state are likely to be unique among various connexin isoforms, resulting from differences in inter-domain interactions between the NT and TM1/TM2 domains and physiological conditions. Indeed, recent cryo-EM structures of Cx26 GJ channels (Khan et al. 2020) and Cx31.3 hemichannels (Lee et al. 2020) resolve NT domains that adopt different orientations as compared to Cx46/50. However, differences in experimental conditions among these studies make direct comparisons challenging (e.g. the presence of lipids inside the pore of Cx31.1).

### Role of NT and the 9th residue in V<sub>i</sub> gating of Cx46/50

Both Cx46 and Cx50 GJs displayed prominent  $V_i$  gating in the range of tested  $V_i$  values ( $\pm 20$  to  $\pm 100$  mV) that could be well described by a two-state Boltzmann equation for each  $V_i$  polarity. A classic voltage gating model for voltage-gated ion channels is that during the gating process, a change in the voltage results in movement of charge or a re-orientation of dipoles (the voltage sensor) relative to the electric field, which leads to either closing or opening of the channel (Bezanilla, 2000). In the case of several GJ channels, the sensor for  $V_i$  gating is believed to reside in the pore lining residues (Harris et al. 1981; Bukauskas & Verselis, 2004; Bargiello & Brink, 2009). In Cx32, charge substitutions up to the first 10 residues of the NT domain have been shown to influence  $V_i$ sensing (Purnick et al. 2000). Charge reversal of E9/E13 of Cx40 has also been shown to alter V<sub>i</sub> sensing (Musa et al. 2004). However, reversal of both K9/K13 of Cx43 showed no effect on  $V_i$  sensing, but did alter residual conductance properties (Musa et al. 2004). We show here that removing a positively charged residue in the pore lining NT domain of Cx46 by the variant R9N showed no change in the  $V_i$  gating sensitivity (A, a Boltzmann parameter can be converted into gating charge, z) and in the half deactivation  $V_i$  ( $V_0$ ). These results indicate that (1) the positive charge on R9 is unlikely to play a role in  $V_i$  sensing or  $V_i$  gating in Cx46 GJs, and (2) there is no change in the free energy difference ( $\Delta G_0 = zFV_0$ ) between aggregated open and closed states in the absence of a voltage field (Yifrach & MacKinnon, 2002; Sukhareva et al. 2003; Xin et al. 2012). We suggest that the lack of a voltage-sensing role for R9 in Cx46 may be due to the charge-neutralizing salt bridge interactions formed by R9 and E12 of neighbouring subunits (see Fig. 2).

In contrast to the findings on Cx46-R9N, the introduction of a positive charge to the NT in both Cx50-46NT and Cx50-N9R GJs resulted in nearly complete loss of their  $V_i$  gating with very little  $V_i$ -dependent deactivation on macroscopic junctional currents (see Fig. 5). We believe that the underlying mechanisms of their apparent loss of  $V_i$  gating are different based on their single channel gating properties. In the case of Cx50-46NT GJ, the single channel currents  $(i_i \text{ values})$  showed long stable opening for all our tested  $V_i$  values with very brief transitions to a residual or closed state. The open probability of Cx50-46NT was approximately 1 with a longer dwell time. The closed or residual states of Cx50-46NT were not observed unless at the highest  $V_i$  values ( $\pm 100 \text{ mV}$ ). These experimental observations are consistent with our proposed model that switching the NT of Cx46 into Cx50 (Cx50-46NT) stabilizes the open state of the GJ channel. However, in the case of Cx50-N9R GJs, the opposite effects on  $i_i$  were observed with reduced open stability (a much shorter open dwell time than wildtype Cx50) and low  $P_{\text{open}}$ levels for all tested  $V_i$  values without any  $V_i$  dependence (Fig. 6). In addition, long-lived residue states were lost in Cx50-N9R GJ and during the entire  $V_i$  pulses, the  $i_i$ values displayed frequent transitions from closed state to two open states (see Fig. 7A and C). These data support a model where the Cx50-N9R GJs in our experimental conditions are already gated (or not recovered from the  $V_i$ -dependent deactivation during the  $V_i$  pulse interval), characterized by a fully closed state and frequent transitions to short-lived open states. Consistent with this model, we observed significant gating of Cx50-N9R GJ during their first large  $V_i$  exposure, not the subsequent  $V_i$  values (B. Yue and D. Bai, unpublished observations). Further experiments are needed to test these models fully. It is notable that equivalent mutation (N9R) in rodent or chick Cx50 displayed prominent  $V_i$  gating with altered gating parameters (Tong et al. 2004; Xin et al. 2010), unlike what we observed here in the sheep Cx50. The NT domains of these orthologues are well conserved. Therefore, it is likely that these species-specific differences are due to unique sequence variations within other regions of the channel that may influence  $V_i$  gating properties.

### Mechanistic differences in single channel conductance for Cx46 and Cx50 GJs

Previous studies have implicated the NT domain and in particular the 9th residue position as being responsible for major differences in single channel conductance  $(\gamma_i)$ in the two closely related isoforms, Cx46 and Cx50 (Tong et al. 2004, 2013; Srinivas et al. 2005; Xin et al. 2010; Xin & Bai, 2013; Myers et al. 2018). We observed that wildtype and variant GJ channels studied here displayed much higher free energy barriers at the NT domain for Cl<sup>-</sup> (the major intracellular anion) versus K<sup>+</sup> (the major intracellular cation), making these GJs more permeable to cations, with a difference in free energy barriers  $\Delta \Delta G_{\text{(Cl--K+)}} = \sim 2.4 - 3.7 \text{ kcal/mol}$ , consistent with previous electrophysiology studies conducted on rodent Cx50 and Cx46 that demonstrate K+/Cl- permeability ratios  $(P_{K+}/P_{Cl-})$  of  $\sim 7/1$  (Trexler *et al.* 1996, 2000; Srinivas *et al.* 1999; Tong et al. 2014). At the same time, the differences in the peak free energy barrier to K<sup>+</sup> permeation between Cx50 and Cx46 ( $\Delta\Delta G_{K+} = 0.82$  kcal/mol) is consistent with the relative differences in  $\gamma_i$  for these isoforms, where we showed sheep Cx50 displays higher  $\gamma_i$  compared to Cx46 (208 pS vs. 166 pS, respectively). This energetic difference appears to be primarily related to the positive charge of R9 in Cx46. While R9 appears to also form a constriction site in the cryo-EM structure of Cx46 that could contribute to the formation of an energetic barrier, this residue equilibrates during MD simulation to form a dynamic ensemble of inter-subunit interactions with E12 and/or R9 of a neighbouring subunit that prevents

this large residue from narrowing the pore permeation pathway (see Figs 1 and 2).

The free energy landscape to cation permeation was found to be similar among our designed GJ variants, depending on the presence or absence of a positively charged arginine at the 9th position. For example, the peak  $\Delta$   $G_{K+}$  for the variants Cx46-R9N and Cx46-50NT were both reduced to that of Cx50, and the peak  $\Delta$   $G_{K+}$  for Cx50-N9R and Cx50-46NT variants were increased to a degree that was similar to Cx46 and displayed similar R9 conformational dynamics (see Figs 2 and 3). By functional comparison, our dual patch clamp data on these variants demonstrate that the  $\gamma_i$  values of these variants displayed unitary conductances  $(\gamma_i)$  in order from high to low: Cx46-R9N (261 pS) > Cx50 (208 pS) > Cx46 (166 pS)> Cx50-46NT (119 pS) = Cx50-N9R (116 pS), while Cx46-50NT was non-functional (discussed above). These results are consistent with free energy calculations obtained by MD, at least on a qualitative level.

Despite this overall congruence, some functional features displayed by the designed variants were not readily explained by the structural data, which may reflect additional structural differences between Cx46 and Cx50 that will require further investigation, and/or reflect the inherent limitations of the models and/or force fields used for MD. For example,  $\gamma_i$  of Cx46-R9N was surprisingly much higher than that of Cx50 and the  $\gamma_i$  values of Cx50-N9R and Cx50-46NT were much lower than that of Cx46. Of note, previous studies that swapped the NT domains of orthologous Cx50 and Cx46 GJs and hemichannels reported similar behaviour (Tong et al. 2004; Tong & Ebihara, 2006; Kronengold et al. 2012). We suggest a mechanistic basis for this observation is most likely due to other differences between these isoforms located within the pore-lining domains of TM1/EC1 that further modulate the conductance properties of these channels (Trexler et al. 2000; Kronengold et al. 2003; Hu et al. 2006; Tong et al. 2013, 2015). Consistent with these results, we do find isoform-specific differences in the K<sup>+</sup> PMF observed within these regions of the channel, although these have proven more difficult to deconvolute (see Fig. 3) (Myers et al. 2018). Indeed, in the study by Kronengold et al. (2012), the NT domain and TM1/EC1 domains were swapped between Cx50 and Cx46 hemichannels, which resulted in chimeras that produced unitary conductance values that were nearly identical to the corresponding wildtype channels from which the NT-TM1-EC1 domains were derived.

Another surprising result was that in our study Cx50-46NT displayed the smallest single channel conductance, despite the results of MD simulation that suggest this chimera forms a larger pore diameter than other variants (e.g. as compared to Cx50-N9R). Again, the mechanistic basis for this observation is not entirely clear, as R9 in this construct was found to adopt

the same population of stabilizing salt bridge interactions as observed for wildtype Cx46 (e.g. 48% vs. 47% in h-bonding distance to E12, respectively) that prevent this residue from narrowing the pore permeation pathway (see Fig. 2). Other reasons for the quantitative differences between experiment and simulation could be due to one or combinations of the following factors: (1) contributions to channel conductance not captured by our structural models (e.g. CL and CT domains were not modelled due to intrinsic disorder of these domains); (2) the cation/anion permeation ratio could be altered by the variants; or (3) inherent limitations in the force fields and/or timescales used for MD simulation. Future experiments are needed to resolve some of these possibilities.

### **Concluding remarks**

Our integrative structural and functional approach was able to provide detailed mechanistic insights on how Cx46 and Cx50 GJs control ion permeation, gating and open state stability, and demonstrate how nuanced differences in the NT domains of Cx50 and Cx46 lead to significantly different channel properties. We uncovered previously under-appreciated roles of hydrophobic anchoring and inter-subunit cooperative interactions (e.g. between R9 and E12) as probable contributors to defining these channel properties. Understanding these differences at a mechanistic level are important to developing our understanding of how various connexins have adapted to their unique physiological roles throughout the body, and how aberrancies introduced by mutation lead to disease. Indeed, the NT domains of Cx46 and Cx50 are hotspots of genetic variation associated with congenital cataracts (Beyer et al. 2013; Mackay et al. 2014; Micheal et al. 2018; Zhang et al. 2018; Ye et al. 2019). A similar integrative approach will be key to providing mechanistic insights into the aetiology of these and other cataract-associated variants and possibly other connexin-linked diseases. Lastly, we note that during the completion of this manuscript, we reported refined structural models of sheep Cx46 and Cx50 that were resolved to 1.9 Å resolution using cryo-EM, in a near-native lipid environment (Flores et al. 2020). These refined models provide an unprecedented level of detail for the connexin family of intercellular communication channels, and are expected to allow even more detailed investigations targeted at understanding the mechanistic principles underpinning the functional differences of these and other closely related GJ channels.

### References

Aasen T, Mesnil M, Naus CC, Lampe PD & Laird DW (2016). Gap junctions and cancer: communicating for 50 years. *Nat Rev Cancer* 16, 775–788.

- Bai D, Yue B, Aoyama H (2018) Crucial motifs and residues in the extracellular loops influence the formation and specificity of connexin docking. *Biochimica et Biophysica Acta (BBA) Biomembranes*, **1860** (1), 9–21.
- Bargiello T & Brink P (2009). Voltage-gating mechanisms of connexin channels. In *Connexins: A Guide*, ed. Harris AL & Locke D, pp. 103–128. Humana Press, Totowa, NJ.
- Beyer EC, Ebihara L & Berthoud VM (2013). Connexin mutants and cataracts. *Front Pharmacol* **4**, 43.
- Bezanilla F (2000). The voltage sensor in voltage-dependent ion channels. *Physiol Rev* **80**, 555–592.
- Bukauskas FF, Kreuzberg MM, Rackauskas M, Bukauskiene A, Bennett MV, Verselis VK & Willecke K (2006). Properties of mouse connexin 30.2 and human connexin 31.9 hemichannels: implications for atrioventricular conduction in the heart. *Proc Natl Acad Sci U S A* **103**, 9726–9731.
- Bukauskas FF & Verselis VK (2004). Gap junction channel gating. *Biochim Biophys Acta* **1662**, 42–60.
- Delmar M, Laird DW, Naus CC, Nielsen MS, Verselis VK & White TW (2017). Connexins and disease. *Cold Spring Harb Perspect Biol* **10**, a029348.
- Flores JA, Haddad BG, Dolan KA, Myers JB, Yoshioka CC, Copperman J, Zuckerman DM & Reichow SL (2020). Connexin-46/50 in a dynamic lipid environment resolved by CryoEM at 1.9 A. *Nat Commun* 11, 4331.
- Garcia IE, Prado P, Pupo A, Jara O, Rojas-Gomez D, Mujica P, Flores-Munoz C, Gonzalez-Casanova J, Soto-Riveros C, Pinto BI, Retamal MA, Gonzalez C & Martinez AD (2016). Connexinopathies: a structural and functional glimpse. *BMC Cell Biol* 17, 17.
- Goodenough DA & Paul DL (2009). Gap junctions. *Cold Spring Harb Perspect Biol* 1, a002576.
- Harris AL, Spray DC & Bennett MV (1981). Kinetic properties of a voltage-dependent junctional conductance. *J Gen Physiol* 77, 95–117.
- Hu X, Ma M & Dahl G (2006). Conductance of connexin hemichannels segregates with the first transmembrane segment. *Biophys J* **90**, 140–150.
- Huang J & MacKerell AD, Jr (2013). CHARMM36 all-atom additive protein force field: validation based on comparison to NMR data. *J Comput Chem* **34**, 2135–2145.
- Humphrey W, Dalke A & Schulten K (1996). VMD: visual molecular dynamics. *J Mol Graph* **14**, 33–38, 27–38.
- Jassim A, Aoyama H, Ye WG, Chen H & Bai D (2016). Engineered Cx40 variants increased docking and function of heterotypic Cx40/Cx43 gap junction channels. J Mol Cell Card 90, 11–20.
- Jurrus E, Engel D, Star K, Monson K, Brandi J, Felberg LE, Brookes DH, Wilson L, Chen J, Liles K, Chun M, Li P, Gohara DW, Dolinsky T, Konecny R, Koes DR, Nielsen JE, Head-Gordon T, Geng W, Krasny R, Wei GW, Holst MJ, McCammon JA & Baker NA (2018). Improvements to the APBS biomolecular solvation software suite. *Protein Sci* 27, 112–128.
- Khan AK, Jagielnicki M, McIntire WE, Purdy MD, Dharmarajan V, Griffin PR & Yeager M (2020). A steric "Ball-and-Chain" mechanism for pH-mediated regulation of gap junction channels. *Cell Rep* **31**, 107482.

- Kim MS, Gloor GB & Bai D (2013). The distribution and functional properties of Pelizaeus-Merzbacher-like disease-linked Cx47 mutations on Cx47/Cx47 homotypic and Cx47/Cx43 heterotypic gap junctions. *Biochem J* **452**, 249–258.
- Koval M, Molina SA & Burt JM (2014). Mix and match: investigating heteromeric and heterotypic gap junction channels in model systems and native tissues. FEBS Lett 588, 1193–1204.
- Kronengold J, Srinivas M & Verselis VK (2012). The N-terminal half of the connexin protein contains the core elements of the pore and voltage gates. *J Membr Biol* **245**, 453–463.
- Kronengold J, Trexler EB, Bukauskas FF, Bargiello TA & Verselis VK (2003). Pore-lining residues identified by single channel SCAM studies in Cx46 hemichannels. *Cell Commun Adhes* **10**, 193–199.
- Kwon T, Harris AL, Rossi A & Bargiello TA (2011). Molecular dynamics simulations of the Cx26 hemichannel: evaluation of structural models with Brownian dynamics. *J Gen Physiol* 138, 475–493.
- Lee HJ, Jeong H, Hyun J, Ryu B, Park K, Lim HH, Yoo J & Woo JS (2020). Cryo-EM structure of human Cx31.3/GJC3 connexin hemichannel. *Sci Adv* **6**, eaba4996.
- Mackay DS, Bennett TM, Culican SM & Shiels A (2014). Exome sequencing identifies novel and recurrent mutations in GJA8 and CRYGD associated with inherited cataract. *Hum Genomics* **8**, 19.
- Maeda S, Nakagawa S, Suga M, Yamashita E, Oshima A, Fujiyoshi Y & Tsukihara T (2009). Structure of the connexin 26 gap junction channel at 3.5 A resolution. *Nature* **458**, 597–602.
- Micheal S, Niewold ITG, Siddiqui SN, Zafar SN, Khan MI & Bergen AAB (2018). Delineation of novel autosomal recessive mutation in GJA3 and autosomal dominant mutations in GJA8 in Pakistani congenital cataract families. *Genes* **9**, 112.
- Moreno AP, Berthoud VM, Perez-Palacios G & Perez-Armendariz EM (2005). Biophysical evidence that connexin-36 forms functional gap junction channels between pancreatic mouse beta-cells. *Am J Physiol Endocrinol Metab* **288**, E948–956.
- Musa H, Fenn E, Crye M, Gemel J, Beyer EC & Veenstra RD (2004). Amino terminal glutamate residues confer spermine sensitivity and affect voltage gating and channel conductance of rat connexin40 gap junctions. *J Physiol* 557, 863–878
- Myers JB, Haddad BG, O'Neill SE, Chorev DS, Yoshioka CC, Robinson CV, Zuckerman DM & Reichow SL (2018). Structure of native lens connexin 46/50 intercellular channels by cryo-EM. *Nature* **564**, 372–377.
- Oh S, Rivkin S, Tang Q, Verselis VK & Bargiello TA (2004). Determinants of gating polarity of a connexin 32 hemichannel. *Biophys J* **87**, 912–928.
- Oh S, Rubin JB, Bennett MV, Verselis VK & Bargiello TA (1999). Molecular determinants of electrical rectification of single channel conductance in gap junctions formed by connexins 26 and 32. *J Gen Physiol* **114**, 339–364.

- Oshima A, Tani K, Hiroaki Y, Fujiyoshi Y & Sosinsky GE (2007). Three-dimensional structure of a human connexin26 gap junction channel reveals a plug in the vestibule. *Proc Natl Acad Sci U S A* **104**, 10034–10039.
- Oshima A, Tani K, Toloue MM, Hiroaki Y, Smock A, Inukai S, Cone A, Nicholson BJ, Sosinsky GE & Fujiyoshi Y (2011). Asymmetric configurations and N-terminal rearrangements in connexin26 gap junction channels. *J Mol Biol* **405**, 724–735.
- Paul DL, Ebihara L, Takemoto LJ, Swenson KI & Goodenough DA (1991). Connexin46, a novel lens gap junction protein, induces voltage-gated currents in nonjunctional plasma membrane of *Xenopus* oocytes. *J Cell Biol* 115, 1077–1089.
- Peracchia C & Peracchia LL (2005). Inversion of both gating polarity and CO<sub>2</sub> sensitivity of voltage gating with D3N mutation of Cx50. *Am J Physiol Cell Physiol* **288**, C1381–1389.
- Pettersen EF, Goddard TD, Huang CC, Couch GS, Greenblatt DM, Meng EC & Ferrin TE (2004). UCSF Chimera–a visualization system for exploratory research and analysis. *J Comput Chem* **25**, 1605–1612.
- Phillips JC, Braun R, Wang W, Gumbart J, Tajkhorshid E, Villa E, Chipot C, Skeel RD, Kale L & Schulten K (2005). Scalable molecular dynamics with NAMD. *J Comput Chem* **26**, 1781–1802.
- Purnick PE, Oh S, Abrams CK, Verselis VK & Bargiello TA (2000). Reversal of the gating polarity of gap junctions by negative charge substitutions in the N-terminus of connexin 32. *Biophys J* **79**, 2403–2415.
- Ramanan SV, Brink PR, Varadaraj K, Peterson E, Schirrmacher K & Banach K (1999). A three-state model for connexin37 gating kinetics. *Biophys J* **76**, 2520–2529.
- Saez JC, Berthoud VM, Branes MC, Martinez AD & Beyer EC (2003). Plasma membrane channels formed by connexins: their regulation and functions. *Physiol Rev* **83**, 1359–1400.
- Sakai R, Elfgang C, Vogel R, Willecke K & Weingart R (2003). The electrical behaviour of rat connexin46 gap junction channels expressed in transfected HeLa cells. *Pflugers Arch* **446**, 714–727.
- Santos-Miranda A, Chen H, Chen RC, Odoko-Ishimoto M, Aoyama H & Bai D (2020). The amino terminal domain plays an important role in transjunctional voltage-dependent gating kinetics of Cx45 gap junctions. *J Mol Cell Cardiol* **143**, 71–84.
- Shearer D, Ens W, Standing K & Valdimarsson G (2008). Post-translational modifications in lens fiber connexins identified by off-line-HPLC MALDI-quadrupole time-of-flight mass spectrometry. *Invest Ophthalmol Vis Sci* **49**, 1553–1562.
- Smart OS, Neduvelil JG, Wang X, Wallace BA & Sansom MS (1996). HOLE: a program for the analysis of the pore dimensions of ion channel structural models. *J Mol Graph* **14**, 354–360, 376.
- Sohl G & Willecke K (2004). Gap junctions and the connexin protein family. *Cardiovasc Res* **62**, 228–232.
- Sosinsky GE & Nicholson BJ (2005). Structural organization of gap junction channels. *Biochim Biophys Acta* **1711**, 99–125.
- Spray DC, Harris AL & Bennett MV (1981). Equilibrium properties of a voltage-dependent junctional conductance. *J Gen Physiol* 77, 77–93.

- Srinivas M, Costa M, Gao Y, Fort A, Fishman GI & Spray DC (1999). Voltage dependence of macroscopic and unitary currents of gap junction channels formed by mouse connexin50 expressed in rat neuroblastoma cells. *J Physiol* **517** 673–689.
- Srinivas M, Kronengold J, Bukauskas FF, Bargiello TA & Verselis VK (2005). Correlative studies of gating in Cx46 and Cx50 hemichannels and gap junction channels. *Biophys J* **88**, 1725–1739.
- Sukhareva M, Hackos DH & Swartz KJ (2003). Constitutive activation of the Shaker Kv channel. *J Gen Physiol* **122**, 541–556.
- Sun Y, Yang YQ, Gong XQ, Wang XH, Li RG, Tan HW, Liu X, Fang WY & Bai D (2013). Novel germline GJA5/connexin40 mutations associated with lone atrial fibrillation impair gap junctional intercellular communication. *Hum Mutat* 34, 603–609.
- Tong JJ & Ebihara L (2006). Structural determinants for the differences in voltage gating of chicken Cx56 and Cx45.6 gap-junctional hemichannels. *Biophys J* **91**, 2142–2154.
- Tong JJ, Liu X, Dong L & Ebihara L (2004). Exchange of gating properties between rat cx46 and chicken cx45.6. *Biophys J* **87**, 2397–2406.
- Tong JJ, Sohn BC, Lam A, Walters DE, Vertel BM & Ebihara L (2013). Properties of two cataract-associated mutations located in the NH2 terminus of connexin 46. *Am J Physiol Cell Physiol* **304**, C823–832.
- Tong X, Aoyama H, Sudhakar S, Chen H, Shilton BH & Bai D (2015). The first extracellular domain plays an important role in unitary channel conductance of Cx50 gap junction channels. *PLoS One* **10**, e0143876.
- Tong X, Aoyama H, Tsukihara T & Bai D (2014). Charge at the 46th residue of connexin50 is crucial for the gap-junctional unitary conductance and transjunctional voltage-dependent gating. *J Physiol* **592**, 5187–5202.
- Trexler EB, Bennett MV, Bargiello TA & Verselis VK (1996). Voltage gating and permeation in a gap junction hemichannel. *Proc Natl Acad Sci U S A* **93**, 5836–5841.
- Trexler EB, Bukauskas FF, Kronengold J, Bargiello TA & Verselis VK (2000). The first extracellular loop domain is a major determinant of charge selectivity in connexin46 channels. *Biophys J* **79**, 3036–3051.
- Veenstra RD, Wang HZ, Beyer EC, Ramanan SV & Brink PR (1994). Connexin37 forms high conductance gap junction channels with subconductance state activity and selective dye and ionic permeabilities. *Biophys J* **66**, 1915–1928.
- Vernon RM, Chong PA, Tsang B, Kim TH, Bah A, Farber P, Lin H & Forman-Kay JD (2018). Pi–Pi contacts are an overlooked protein feature relevant to phase separation. *eLife* 7, e31486.
- Verselis VK, Ginter CS & Bargiello TA (1994). Opposite voltage gating polarities of two closely related connexins. *Nature* **368**, 348–351.
- Villanelo F, Escalona Y, Pareja-Barrueto C, Garate JA, Skerrett IM & Perez-Acle T (2017). Accessing gap-junction channel structure-function relationships through molecular modeling and simulations. *BMC Cell Biol* **18**, 5.

- Wang Z & Schey KL (2009). Phosphorylation and truncation sites of bovine lens connexin 46 and connexin 50. *Exp Eye Res* **89**, 898–904.
- White TW, Bruzzone R, Goodenough DA & Paul DL (1994*a*). Voltage gating of connexins. *Nature* **371**, 208–209.
- White TW, Bruzzone R, Wolfram S, Paul DL & Goodenough DA (1994*b*). Selective interactions among the multiple connexin proteins expressed in the vertebrate lens: the second extracellular domain is a determinant of compatibility between connexins. *J Cell Biol* 125, 879–892.
- Williams WA (1991). *Statistical Methods (8th ed.)*, vol. **86**. American Statistical Association, Alexandria, VA.
- Xin L & Bai D (2013). Functional roles of the amino terminal domain in determining biophysical properties of Cx50 gap junction channels. *Front Physiol* **4**, 373.
- Xin L, Gong XQ & Bai D (2010). The role of amino terminus of mouse Cx50 in determining transjunctional voltage-dependent gating and unitary conductance. *Biophys J* **99**, 2077–2086.
- Xin L, Nakagawa S, Tsukihara T & Bai D (2012). Aspartic acid residue D3 critically determines Cx50 gap junction channel transjunctional voltage-dependent gating and unitary conductance. *Biophys J* **102**, 1022–1031.
- Ye Y, Wu M, Qiao Y, Xie T, Yu Y & Yao K (2019). Identification and preliminary functional analysis of two novel congenital cataract associated mutations of Cx46 and Cx50. *Ophthal Genet* **40**, 428–435.
- Yifrach O & MacKinnon R (2002). Energetics of pore opening in a voltage-gated K<sup>+</sup> channel. *Cell* **111**, 231–239.
- Zhang L, Liang Y, Zhou Y, Zeng H, Jia S & Shi J (2018). A missense mutation in GJA8 encoding connexin 50 in a Chinese pedigree with autosomal dominant congenital cataract. *Tohoku J Exp Med* **244**, 105–111.
- Zonta F, Buratto D, Cassini C, Bortolozzi M & Mammano F (2014). Molecular dynamics simulations highlight structural and functional alterations in deafness-related M34T mutation of connexin 26. *Front Physiol* 5, 85.

### **Additional information**

### Data availability statement

Data and expression vectors related to the electrophysiology experiments presented in this work will be made available upon request. For MD data, raw, un-aligned protein and ion trajectories have been deposited at Zenodo (https://doi.org/10.5281/zenodo.4625961). In-house codes developed for analysis of MD trajectory data have been deposited at GitHub (https://github.com/reichow-lab/Yue-Haddad\_et-al.JPhysiol).

### **Competing interests**

None declared.

#### **Author contributions**

All authors contributed to the preparation of the manuscript and approved the final version. B.Y. and B.G.H. contributed equally. B.Y. designed, performed and analysed patch clamp experiments. H.C. designed and generated all variants and designed and performed GFP-tagged Cx46 variant localization experiments. Z.Z. and M.A. participated in patch clamp experiments, localization experiments, and analysed relevant data. B.G.H. and U.K. developed homology structure models, designed and conducted MD simulations, and performed analysis of MD data. D.M.Z. and S.L.R. supervised the MD studies. D.B supervised the electrophysiology and localization studies. S.L.R. and D.B. provided overall oversight of the design and execution of the work. All authors agree to be accountable for all aspects of the work in ensuring that questions related to the accuracy or integrity of any part of the work are appropriately investigated and resolved. All persons designated as authors qualify for authorship, and all those who qualify for authorship are listed.

### **Funding**

This work was supported by the Natural Sciences and Engineering Research Council of Canada (288241 to D.B.), the National Institutes of Health (R35-GM124779 to S.L.R.; R01-GM115805 to D.M.Z.; F31-EY031580 to B.G.H.) and the National Science Foundation (MCB 1715823 to D.M.Z.; XSEDE EMPOWER, ACI-1548562 to U.K.).

### Keywords

connexin 46, connexin 50, gap junction channel, ion channel, molecular dynamics, open dwell time, patch clamp, single channel conductance

### **Supporting information**

Additional supporting information may be found online in the Supporting Information section at the end of the article.

### **Statistical Summary Document**